Underwater *in situ* optical measurements and coral fluorescence for shallow water remote sensing

by

Eran Fux

Submitted to the Department of Ocean Engineering
in partial fulfillment of the requirements for the degree of

Master of Science in Ocean Engineering

at the

MASSACHUSETTS INSTITUTE OF TECHNOLOGY

June 1996

Author .....
Department of Ocean Engineering
June, 1996

Certified by .....
Dr. Charles H. Mazel
Research Engineer
Thesis Supervisor

Certified by .....
Prof. Henrik Schmidt
Prof. in the Dep. of Ocean Engineering
Thesis Supervisor

Accepted by .....
Prof. A. Douglas Carmichael
Chairman, Graduate Thesis Committee

Underwater *in situ* optical measurements and coral fluorescence for shallow water remote sensing

by

Eran Fux

Submitted to the Department of Ocean Engineering
on June, 1996, in partial fulfillment of the
requirements for the degree of
Master of Science in Ocean Engineering

Abstract

Today's available technology and continuing developments in hyperspectral optical remote sensing for shallow waters are challenging the ability to handle and interpret the data collected. Modern systems' spatial and spectral resolution motivate the need for baseline knowledge of optical properties of the near shore ocean bottom and objects of interest. Data are needed both for ground truthing of instrument performance and for the development of interpretive and predictive models.

A background study is presented to outline the issues to be addressed while developing a shallow water remote sensing system, both from the engineering point of view and the related environmental considerations..

An underwater diver carried spectrometer (BSF - Benthic SpectroFluorometer) was developed and built by Dr. Charles H. Mazel from the OE department at MIT for reflectance and fluorescence measurement. A large part of this work describes the characteristics of the instrument, the wavelength calibration and the spectral radiant output calibration. An automated dark current prediction algorithm which reduces noise in the signal, and improves system performance was developed. The instrument was successfully tested and operated to collect *in situ* data from objects of interest in several field trips.

The contribution of fluorescence to the apparent color of corals was addressed. An experimental method to determine true reflectance of fluorescence enhanced colors is presented. The method was improved and modified for *in situ* color measurements of corals with the BSF. The proposed method will be tested this summer in several field trips.

Thesis Supervisor: Dr. Charles H. Mazel
Title: Research Engineer

Thesis Supervisor: Prof. Henrik Schmidt
Title: Prof. in the Dep. of Ocean Engineering

Contents

List of Figures

0.1 Introduction

Optical remote sensing of coastal shallow waters is gaining an accelerated interest by the scientific community.

Today's available technology and continuing developments in multispectral optical remote sensing for shallow waters are challenging the ability to handle and interpret the data collected. Modern systems' spatial and spectral resolution motivate the need for baseline knowledge of optical properties of the near shore ocean bottom and objects of interest. Data are needed both for ground truthing of instrument performance and for the development of interpretive and predictive models. A library of *in situ* spectral signatures of bottom entities, such as sand, sea grass, corals, rocks etc. is required (Ref. [3]).

To analyze a signal received by a sensor on a remote platform, one needs to follow the light path from the source, through the medium to the sample and finally to the detector, and to observe the affect that each step has on the signal.

The output that an end user of such a system might expect from an ORSS very much depends on the nature of the application:

- Navy-marine forces: Detect, identify and map near shore features of interest.
- Ocean environment preservation: Monitor and detect pollution, marine habitats, bottom properties etc.
- Marine biology: Species distribution, monitoring algae blooms etc.

One might be interested in the optical signature of an underwater mine, while the other might investigate fluorescence effects of tropical reef corals or the population of a jelly-fish in a given water volume. These questions, although seems different from one another, all share the same basic fundamental problems to be addressed.

This work will identify the issues and problems involved with the subject. Furthermore it describes what is the available technology that already exist in the market, as available in the open literature.

I will concentrate on the ocean part of the problem - I will not deal with the problem of the atmospheric attenuation. However it is worth mentioning that due to the location of the area of interest (coast-line), this problem is complicated, and constantly changing in time.

An underwater diver carried spectrometer (BSF - Benthic SpectroFluorometer) was developed and built by Dr. Charles H. Mazel from the OE department at MIT. The instrument was successfully tested and operated to collect reflectance and fluorescence data from objects of interest in several field trips. A major part of my work has been to assist in the design, calibration and operation of the instrument. The BSF is an *in situ* reflectance and fluorescence measurement tool that can be used as a ground truthing tool for an ORSS or as an independent tool for underwater spectral measurements.

In addition, the contribution of fluorescence to apparent color of tropical reef corals was addressed. The study is a part of a larger scale attempt to investigate the meaning of the fluorescence phenomena in coral tissues. An experimental method was used to determine true reflectance curves of fluorescence enhanced colors of fluorescing objects. It is believed that the fluorescence behavior of certain coral species might give information to scientists which will contribute to environmental monitoring of coral reefs. The method will be tested in the next field trip, planned for this summer (1996).

This thesis is divided to three major parts:

- In chapter 1 I present a general overview of the aquatic remote sensing topic. A state of the art sensor is described to demonstrate today's available technology and limitations. Both technological issues and aquatic environmental aspects of the problem are presented.
- Chapter 2 is a description of the BSF instrument, concentrating mainly on the issues that I was involved with: wavelength calibration, dark current correction, sensitivity correction and more.
- In chapter 3 I describe a known experimental method for finding true reflectance spectral distribution for fluorescing surfaces. I also present some improvements to the method, and set the stage to use the improved method in the field.

Chapter 1

Remote sensing background

1.1 Identifying the related problems

Before immersing in the technical details of designing an aquatic remote sensing system, lets consider what issues are be addressed in the process.

- What platform for an ORSS (Optical Remote Sensing System) can be used?
- Passive (using only the ambient available light) vs. active (using a laser beam source) system. In this thesis I will concentrate on passive systems.
- Atmospheric properties: attenuation between the detector and the water surface (one way or two ways, depending if it is an active or a passive system).
- The light going through an air-water interface.
- Water column properties: attenuation as the light path goes through the water at different locations, to different depth.
- In-situ measurements of bottom properties and measurements of different subjects of interest.
- Spectral averaging due to finite, but relatively large data unit (pixel). For example, a reasonable pixel size for an advanced system, at a 1000m flight height can be a square of 1x1m (Ref. [3]).
- Ground Truthing. During the development of the system, results must be verified, and correlation should be found between the analysis and the relevant underwater location.

In the following pages I will present an existing remote sensing system, and I will argue that its technology is already ahead of our present analytical interpretation capability.

1.1.1 Platforms for ORSS

We could think of few different ORSS configurations, mainly depending on the carrying platform:

1. Remotely operated underwater vehicles (ROV).
2. Autonomous underwater vehicles (AUV).
3. Surface vessels.
4. Airborne systems.
5. Satellite systems.

Remotely Controlled Underwater Vehicles

This configuration can also be considered as an *in* situ measurement option. The operator has control of the vehicle, and in real time, can identify items of interest and directly check them. This configuration can be useful when a "surgical approach" is needed, such as wreck search at deep waters, etc. An ROV connected to a surface vessel by cable can get all its power supply and control commands through the cable. However this cable can act as a double edged sword by complicating the operation and limiting the ROV maneuverability.

The ROV is limited in area coverage and operation in shallow waters, thus I will not consider it as a useful independent ORSS. However, during the development of a productive ORSS, underwater vehicles can be helpful in measuring local properties of subjects and ground truthing.

Autonomous Underwater Vehicles

Although an AUV can be programmed to thoroughly cover a reasonably wide area, today this range is measured in few miles, and not in tens or hundreds of miles. For some applications this configuration can be good enough (for example, open ocean measurements), however the logistics involved in such an operation is complicated and the volume of data needed for imaging can not be retrieved in real time (or close to real time).

An underwater vehicle (AUV or ROV), has the advantage of being able to go as deep as it needs to the location of interest, but has a strong disadvantage in the shallow waters where some applications might have the strongest interest, especially when referring to near coast line applications. The combination of bottom topology (reefs, rocks etc.), waves and currents can make the operation of systems such as AUVs and ROVs extremely difficult.

The future may hold new possibilities for the use of AUV's and ROV's as a remote sensing platforms, as their development progresses, but at present this is not a practical solution for wide area coverage. In this thesis I will consider the operation

of AUVs and ROVs as an optional aid tool for an airborne system, mainly during the development phase.

Surface Vessels

The same area coverage arguments given to the AUV operation can apply also in this case. In addition the surface vessel stability might add to the complexity of the problem, and for some applications (mainly of a military nature) surface vessels (as ROVs) are out of the question.

A surface operation is limited to the surface only, and thus inferior to the operation of an AUV or ROV. It is generally accepted that this is not a good configuration for an optical system.

Airborne Systems

Although there are still many problems to solve, this configuration seems to be the best fit to a near coast line ORSS. An airplane is big enough to meet any spatial requirement that an ORSS might have, and there are no power supply problems which are unsolvable since any reasonable power demand can be produced onboard. An airplane can carry not only the ORSS, but also supporting systems (for example, a cooling system for a laser), analyzing equipment for real time response and human operators, if required. This is a fast platform that can cover a wide range in a relatively short time, operational response time can be short (i.e. the time that passes between the decision to analyze a given location to the actual data collection). Data separation (pixel resolution) can be controlled by flight height and system sensitivity, and data can be processed in real time. One might also think of a small, remotely controlled drone as a platform for an ORSS, where some of the above arguments will not hold, but for other reasons might be preferable.

However, an airborne platform can also introduce new problems to the already complicated task such as high frequency vibrations, safety of flight regulations etc. Nevertheless, these disadvantages are by far dominated by the optional advantages.

Satellite Systems

Although such a system is tempting due to its huge area coverage, it is not applicable for an ordinary use of an ORSS, for coast line operation (more details in the next section). There are a few crucial points that will make the use of such a system very difficult:

- Resolution is not good enough for useful analysis (pixel size of tens of meters).
- Availability of platforms is very limited.
- Very high cost operation.
- Spectral resolution is limited compared with the existing airborne systems.

These systems gained their respectable place in the oceanographic optical remote sensing arena. However, for the high resolution needs of near coastal applications they are not sensitive enough. It is my guess that the future will show improvements and development in the satellite system sensors which will open the discussion about their applicability.

1.1.2 Different Altitude Systems

Low altitude (100-500m) systems

In this section of instruments, Kirk (Ref. [1]) consider only linear path systems, i.e. those which do not scan from side to side simultaneously. If a spectrometer is used to measure radiance, it should complete its scan quickly to minimize the effects of changes in the emergent flux from point to point along the aircraft path. Different systems, for different applications were built. For example Neville and Gower (1977) used a spectroradiometer design by Walker (1974), in which the spectrum produced by a diffraction grating was distributed over an array of 256 silicon diodes. It was possible to read out a complete spectrum (380-1065 nm), at two second intervals. A different type of system was designed by Arvesen, Millard and Weaver (1973) who developed a differential radiometer which carried out simultaneous measurements of upward radiance at 443 nm and 525 nm, and continuously compared them. This had the advantage that changes in incident light or variations of water surface roughness, affected both wavelengths, and thus were eliminated. This system was used to calculate phytoplankton concentration, which affects these wave lengths.

Medium/high altitude systems

A spatial scanning photometer - the Ocean Color Scanner (OCS) was developed by NASA for remote sensing from a U-2 aircraft at altitudes of 18 to 20 km, with 10 spectral bands (433 to 772 nm), and a bandwidth of about 20 nm. It scans by means of rotating mirror at 45^o and uses a telescope with a field of view of about 0.2^o, producing at the U2 operating altitude of 19.8 km a spatial resolution of about 75x75 m.

Another system is the M2S Multispectral Scanner, which was designed for intermediate altitude. It has 10 spectral bands covering the spectrum range of 380 to 1060 nm, with a 40 nm bandwidth. From an altitude of 3 km, the system resolution is an 8m square with an 8.5 km wide swath.

The AAHIS, (an advanced hyperspectral system that will be presented in this paper) also belongs to this group, presenting a modern state of the art system with a spatial resolution of 1x1 m for flight altitude of 1 km and 72 channels with a 5.5 nm bandwidth.

Satellite systems

Few Landsat satellite have been placed in orbit. All of these satellites are carrying an MSS Multispectral Scanner, covering the spectral bands 4,5,6 and 7 (500-600nm,

600-700nm, 700-800nm and 800-1000nm, respectively). The Landsat optical system was primarily designed for remote sensing of terrestrial regions. Its sensitivity is inadequate to detect the variations in reflectance for the ocean surface, and it doesn't cover the important blue (400-500 nm) part of the spectrum.

The latest Landsat carries, as well as the MSS scanner, another scanner known as the Thematic Mapper, which has a band in the blue (450-520 nm), green (520-600 nm), red (630-690 nm) and near infrared (760-900 nm) wavelengths, as well as three bands in the infrared. Its spatial resolution is a 30m square. Although primarily designed for prediction of crop production, it may prove to be valuable also for remote sensing of the aquatic environment.

In 1978 the Nimbus-7 satellite was launched, carrying the Coastal Zone Color Scanner (CZCS) which was designed specially for remote sensing of the aquatic environment. It has four bands in the visible, each 20 nm wide for the following measurements:

430 - 450 nm - Chlorophyll absorption.
510 - 530 nm - Chlorophyll absorption.
540 - 560 nm - CDOM.
660 - 680 nm - Chlorophyll concentration.
700 - 800 nm - Surface vegetation.
1050-1250 nm - Surface temperature.

To avoid sun glitter the sensor can be tilted to scan at up to 20^o from the nadir, ahead or behind the spacecraft. It has a mirror at 45^o rotating in 8.1 rps, directing a telescope which gives an instantaneous field of view of $865 \mu radians$ (0.05^o), producing at the satellite altitude of 955 km, a spatial resolution of 825 m.

A new era in space remote sensing began in Feb. 21 1986, when the French launched the first SPOT program satellite, SPOT-1. This program evolved to be a large international program with ground receiving stations and data distribution outlets located in more than 30 countries. The SPOT-1 was the first earth resource satellite system to include a linear array sensor and employ push-broom scanning techniques. It is also the first system to have pointable optics, which enables side-to-side off-nadir viewing capabilities, and affords full scene stereoscopic imaging from two different satellite tracks. The sensor payload consists of two identical High-Resolution-Visible (HRV) imaging systems and auxiliary magnetic tape recorder. Each HRV is designed to operate in either of two modes of sensing:

1. A 10 m spatial resolution "panchromatic" (black and white) mode over the range 510 to 730 nm.

2. A 20 m spatial resolution, multispectral (color, infrared) mode over the ranges 500 to 590 nm, 610 to 680 nm, and 790 to 890 nm.

Each HRV contains four CCD subarrays. A 6000-elements subarray is used in mode 1, and three 3000-element subarrays are employed in mode 2. Data are encoded over 256 digital number range, and transmitted at a rate of 25 MBpS. Each instrument field of view is 4.13^o, such that the ground swath of each HRV scene is 60 km under nadir viewing conditions. A plane mirror which can be rotated at ground command

through an angle of $+/-27^o$, allows each sensor to image any point within a strip extending 475 km to either side of the satellite ground track.

However, for the specific shallow water applications needs that I mentioned before, even this resolution is not fine enough, although it is very powerful for oceanographic applications.

1.2 Hyperspectral Remote Sensing System

For shallow water remote sensing applications, we need high spatial resolution, to be able to analyze small entities such as coral heads, man maid objects etc. We also want to have as much optical information about the scene as we can get, thus a high spectral resolution is desired as well. Hopefully, when we are able to define exactly what is the data the one needs, in order to solve the problem in question, maybe we wouldn't need to cover the full spectrum. However, at this point of our knowledge we need a tool that can detect as much as possible.

Hyperspectral imaging (HSI) is the technique of imaging a scene in many color bands, so that a complete spectrum is recorded at each spatial location in the image (pixel). HSI is distinguished by the number of spectral bands recorded (tens or hundreds), by the narrowness of each hyperspectral band (typically 10 nm or less), and by the continuous nature of the data.

Such a system is the Advanced Airborne Hyperspectral Imaging System (AAHIS). This is a state-of-the-art system that was developed by SETS Technology, Inc. (Ref. [3]), that is still undergoing development, but already operational for commercial use.

1.2.1 Description of the sensor

The AAHIS consists of the following: the imaging spectrometer, the spectrometer vibration isolation mount, the spectrometer focal plane array and its controller, a scene monitor camera with video monitor and SVHS VCR, and a computer with hard disk and a 5GB tape drive (Refer to block diagram in Figure 1-1).

The AAHIS sensor is a "pushbroom" type imager which builds an image line-by-line. The sensor foreoptics images the scene onto the entrance slit of the spectrometer, so that only light from single narrow image line oriented perpendicular to the direction of motion of the sensor is allowed to pass into the spectrometer. Inside the spectrometer, this polychromatic line image is simultaneously dispersed into a two dimensional spectrum and re-imaged onto the focal plane array. As the aircraft moves forward over the scene, the image of the slit scans the terrains bellow, and the strip image is built up line-by- line, producing a hyperspectral "data cube" consisting of a stack of up to 288 monochromatic images.

Spectral information is collected simultaneously in 288 separate bands, equally spaced between 433.7 nm (blue-violet) and 830.9 nm (near infrared), to yield a band width of 1.38 nm. In practice these spectral data are combined on the CCD chip to allow 72 channels, each 5.46 nm wide, spaced equally between 435.8-828.8 nm.

Spatial resolution is determined by the sensor field of view, the spectrograph aberration and frame rate, ground speed and altitude of the aircraft. At an altitude of 1,000m, ground speed of 79 knots and rate of 40 frames/sec. (typical data collection values), the system spatial resolution is 1m, which yields a pixel size of 1x1m). Under these conditions data is recorded at a rate of 1.1 MB/sec. which is well within a SCSI II interface capability. The AAHIS sensor is controlled by a Macintosh Quadra800 with 36 MB RAM, so approximately 1200 frames (30 seconds of data at 40 frame/sec.)

may be collected in an uninterrupted sequence before data must be downloaded to the 5 GB magnetic tape.

A standard color video camera supplies a video signal to a monitor, allowing the operator to view in real time the same ground scene which the sensor measures. This image is also recorded on a VCR, and a time base is added to the tape. The AAHIS is mounted to the aircraft on vibration isolation mounts, while the sensor and the camera are precisely boresighted looking down through a windowless hole in the floor.

1.2.2 Hyperspectral Imaging for Marine Applications

Hyperspectral imaging (all colors simultaneously) is more effective than panchromatic imaging (imaging at one broad band spectral channel) for detection and identification of the materials composing objects and events of interest. All materials reflect radiation across the electromagnetic spectrum in ways often unique for each material, forming a unique spectral signature.

The fundamental benefit of spectral imaging is the ability to utilize spectral (color) information from objects in a scene to distinguish and discriminate those objects. A spectrum can be extracted for each pixel in a scene. The data cube, related to a measured scene, can be processed and analyzed as an entire cube or as individual monochromatic or polychromatic images and spectra.

Data collected are processed with an Hyperspectral Image Processing Software (HIPS from *SETS Technology, Inc.*), which is a package running on Sun/UNIX workstations. The HIPS allows the analyst to display a video image, and selectively examine each pixels' spectrum. In order to produce information about the type and compositions visible in an image, and their area distribution, corrections and interpretations algorithms are applied to the data.

1.2.3 Spectral Mixture Analysis

Image classification is a traditional image processing methodology, which produces a map indication with different colors, according to the classification criteria applied. However, according to ref. [3] it is a time consuming process with little efficiency for marine applications. A more robust, physically based method of spectral mixture analysis with a subpixel linear mixing model (LMM) is suggested, using purely spectral characteristics. The radiance of a pixel in band i, R_i, is assumed to be a linear combination of endmember spectra:

$$R_i = \sum_{j=1}^{n} f_j M_{j,i} + r_i \tag{1.1}$$

where f_j is the fraction of the pixel consisting of the radiance of the *jth* endmember in band i, $M_{j,i}$. r_i is the unmodeled radiance for the pixel in band i, and n is the number of endmembers. In most of the LMM implementations:

$$\sum_{j=1}^{n} f_j = 1 \tag{1.2}$$

which implies assuming $r_i = 0$ in this case.

The endmembers $M_{j,i}$, can either be references chosen from a spectral library or are selected from within the scene. Each pixel is then assigned the fractional amount of each endmember required to best model the actual pixel spectrum. The end product of LMM are a series of images provide a quantitative characterization of the scene which were built by the materials that create the spectral signatures (limited to the variety of data in the spectral libraries).

The success and accuracy of the procedure is highly dependent on the variety and quality of the library of spectral signatures. **This is the major area to which our *in situ* measurements can contribute.**

1.2.4 Spectra Identification

Examples of spectral extraction are shown in Figure 1-2. Lets concentrate on the "Tree next to pier" spectrum line. Two sets of data are presented: On top, AAHIS derived spectra, and on the bottom, field spectrometer measurement for comparison. (Note: this is an ON LAND target). It can be seen that there is a good agreement in the spectra shapes of the two readings in the wavelength range 450-780 nm. The AAHIS spectra also clearly identify the Chlorophyll peak (679-724 nm). However, we have to remember that these encouraging results which applied to a large, on land target, do not necessarily represent the situation for an underwater target.

In order to better understand the difficulties involved with an aquatic environment, we need to understand the nature of the underwater light field, and the effects of the ocean on the light properties. In the next section I will present a general review of the underwater light field, and then discuss the difficulties that we face while trying to model and analyze the spectral data of an underwater scene.

1.3 The underwater light field

Since we are considering passive systems, we need to follow the light from the source (sun) to the detector, and understand the different phases it is going through: atmospheric attenuation, air-water interface, water column effects, the sample, and back - all the way to the detector. Again, in this thesis I will only discuss the "wet" part of the problem.

1.3.1 Transmission across the air-water interface

The solar radiance must find its way across the air-water interface. Some of it is reflected back, and some penetrates, with a shift in angle. The dependence of reflectance, r, of light on the zenith angle of the incident light in air (θ_a) and the angle to the downward vertical in water (θ_w) is given by Fresnel's Equation:

$$r = \frac{sin^2(\theta_a - \theta_w)}{2sin^2(\theta_a + \theta_w)} + \frac{tan^2(\theta_a - \theta_w)}{2tan^2(\theta_a + \theta_w)}. \tag{1.3}$$

where the angle θ_w is determined by θ_a through Snell's law:

$$\frac{sin\theta_a}{sin\theta_w} = \frac{n_w}{n_a}. \tag{1.4}$$

For our purposes $n_w/n_a = 1.33$ is good enough, however in principle it is a function of temperature, salinity and wavelength. Snell's law works in reverse too, but going from water to air light might be fully reflected back if θ_w is greater than 49°.

The results of the above is summarized in Figure 1-3 where the reflectance of the water surface is given as a function of zenith angle and wind speed (which affects the surface roughness).

1.3.2 Light attenuation in water

In general there are two main mechanisms that contribute to the attenuation of light while propagating through an aquatic medium: absorption and scattering. The general form of aquatic attenuation is given by:

$$E(Z) = E(0)e^{-KZ}, \tag{1.5}$$

where

Z Depth

K Attenuation coefficient.

$E(Z)$ Irradiance at depth Z.

$E(0)$ Irradiance just under the water surface.

To determine the magnitude of k, one needs to understand the contribution of the different parameters to the attenuation coefficient. Many absorption and scattering. These are presented in the following sections:

1.3.3 Absorption of light within the aquatic medium

Essentially all the light absorption which takes place in natural waters is attributed to four components: the water itself, dissolved yellow pigment, photosynthetic pigments and inanimate particulate matter (tripton).

Water

Pure water although appears colorless is in fact a blue liquid. The blue color arises from the fact that it absorbs weakly in the blue and the green regions of the spectrum, but at wavelengths above 550 nm it absorbs significantly. Figure 1-4 shows the absorption spectrum of pure water, based on values from two different sources, that form a continuous spectrum. It is clear that the absorption is very strong starting from about 600 nm, and that infrared wavelengths are almost completely blocked.

Yellow Substance (CDOM, gilvin)

When plant tissue decomposes most of the organic matter is broken by microbial action to carbon dioxide and inorganic forms of nitrogen, sulphur and phosphorus. In the course of the decomposition process compounds referred to as 'humic substances' are formed. Soil chemists classify them into three main fractions on the basis of solubility behavior. The soil is extracted with dilute alkali. The humic material that does not dissolve is called 'humin'. Of the alkali-soluble fraction, some is precipitated. This is called 'humic acid'. The remaining humic material in the solution is called 'fulvic acid'. All three of them are dark brown, where the soluble ones give rise to yellow-brown solutions that gave them their name.

The significance of the soil humic material is that as water, originated as rainfall, drains through soil and into rivers, lakes and ultimately into the ocean, it extracts from the soil some of the humic substances mentioned, and contribute in part a yellow color to the water, with major consequences for the absorption of light, particularly at the blue end of the spectrum. Figure 1-5 shows typical humic substances absorption spectra. The presence of CDOM (Colored Dissolved Organic Matter) in sea water is a function of how close the location is to river mouths, the amount of local rain and ocean currents. In general, collected data show that marine waters have much less dissolved color than inland waters, and the greater the distance from land, the lower the concentration of CDOM is.

Tripton

The inanimate particulate matter, or tripton, is the fraction that is the most difficult to measure, thus it received the least attention. At typical concentrations the material does not absorb light strongly but scatters quite intensely. A method of collecting the material by a filter from a given water volume, then resuspending it in a controlled, smaller volume was developed. The concentrated water are measured, and the original absorption coefficients are calculated from the volume ratio. The tripton absorption spectra have much the same shape as CDOM: absorption is low

at the red, and rises steadily as wavelength decreases into the blue and UV. In turbid waters containing large amounts of suspended material derived from soil erosion in the catchment, or (in shallow waters) wind resuspention of sediments, non-living particulate absorption can exceed absorption due to dissolved color. Figure 1-6 show a comparison of spectral absorption properties of different tripton fractures off the shores of southeast Australia.

Phytoplankton

The absorption of light by the photosynthetic pigments (*chlorophylls, carotenoids, biliprotein*) of the phytoplankton can be substantial. In productive waters, algae may be present in concentrations such that by self-shading they limit their own growth (this is not likely to happen in the ocean, but ruther in fresh, in-land waters). The light absorption properties of phytoplankton populations as they occur in nature are not easy to measure. Most of the available data come from laboratory studies, and thus much research should be done to verify the correlation of the experimental data to the reality. Yentsch (1960) measured the absorption spectra of a natural population of marine phytoplankton off Woods Hole waters, were the cells were a layer on a cleared membrane filter. However, these measurements can not provide in-situ absorption coefficients due to intensification of absorption resulting from multiple scattering within the layer.

It is possible to estimate the absorption coefficient of the medium by comparing two measured sites that have similar scattering coefficients, but known, different phytoplankton populations. Results of such comparison is presented in Figure 1-7.

Total absorption spectra

Finally, summing all the above contributors to the absorption, yields the total absorption coefficient of the water column, for a given water body. Figure 1-8 shows the total absorption coefficients of five Australian waters. The closest to our interest of shallow, coast-line waters is case 'e' (ocean waters), which as expected, shows an increased absorption towards the red in sea waters.

Optical classification of natural waters

It is useful to have some broad identification of the optical character of a water body, without having to fully specify all the inherent optical properties of that location and time of year. Jerlov (1951, 1976) classified marine waters into three types of oceanic waters (I, II, III), and nine of coastal waters (1 to 9). Spectral variation of some of these water types are shown in Figure 1-11 (Table 1). However, Jerlov's measurements, although pioneering, do not always agree with modern submersible spectroradiometer data, thus new classifications were suggested over the years. Pelevin and Rutkovskaya (1977) suggested that ocean waters should be classified in terms of the vertical attenuation coefficient ($log_{10}K_d$), for irradiance at 500 nm, multiplied by 100. Nowadays it is more accepted to use log_e definitions, thus it is logical to modify Pelevin and Rutkovskaya method to log_eK_d.

Kirk (1986) proposed a crude optical classification, applicable mainly to inland waters. He suggested to use different types to describe the main absorption mechanism for the water in question:

- Type G : CDOM (gilvin) absorbs stronger than particulate material, at all wavelengths.
- Type GA: CDOM absorbs stronger than particulate material in short wavelengths and vice-versa near the red.
- Type T : Particulate material (mainly tripton) absorbs stronger than CDOM at all wavelengths.
- Type GT: Absorption by CDOM and by particulate material is roughly the same at all wavelengths.

Marine waters are, apart from the effects of the yearly phytoplankton cycle (in non tropical areas), generally constant in their optical properties, but coastal waters can change their properties, for example after heavy rains that might carry CDOM into the sea.

1.3.4 Scattering of light within the aquatic medium

Scattering is a process where a photon interacts with some component of the medium in a way that it is diverged from its original path. Traditionally, two kinds of scattering are considered - density fluctuation and particle scattering.

Density fluctuation scattering

In any liquid the continual random motion of the molecules leads to localized microscopic fluctuations of density and therefore of the electric constant. The interaction of the radiation field with these inhomogeneities is considered in the Einstein-Smoluchowski theory. The predicted angular distribution of scattering is similar to that given by the Rayleigh theory in gases, i.e. it is identical in the forward and backward directions.

Particle scattering

The Rayleigh and Einstein-Smoluchowski theory apply only when the scattering centers are small compared to the wavelength of light. However, even the purest natural waters, optically speaking, contain high concentrations of particles such as particles derived from land, sediment, phytoplankton, bacteria, dead cells etc. - all of which scatter light.

Mie (1908) developed a theoretical basis for predicting the light scattering behavior of spherical particles. The Mie theory, for very small particles, agrees with the Rayleigh theory, and give solutions for larger particles. However, these solutions are analytically complex and do not allow easy numerical calculations. For particles

larger than the wavelength of the light Mie theory predicts that most of the scattering is in the forward direction (Fig. 1-9).

In the case of particles larger than a few wavelengths of light the mechanism of scattering can be understood on the basis of diffraction and geometrical optics. Calculations by Hodkinson and Greenleaves (1963) for suspension of spherical particles of mixed sizes show that most of the scattering at small angles ($10 - 15^o$) can be attributed to diffraction, whereis most of the scattering at larger angles is due to external reflection and transmission with reflection (Fig. 1-9), where a good agreement with the Mie theory can be seen.

Any particle in a beam of light will scatter a certain fraction of the beam and the radiant flux scattered will be equivalent to that in a certain cross-sectional area of the incident beam. This area is the *scattering cross-section* of the particle. The efficiency factor for scattering, Q_{scat}, is the scattering cross-section divided by the cross-sectional area of the particle. In the case of an absorbing particle, the radiant flux absorbed is equivalent to that in a certain cross-section area of the incident beam. This area is the *absorption cross-section* of the particle. The efficiency factor for absorption, Q_{abs}, is the absorption cross-section divided by the cross-section area of the particle. This leads to the attenuation efficiency factor:

$$Q_{att} = Q_{scat} + Q_{abs}. \tag{1.6}$$

where Q_{att} can be greater than one. That is, a particle can affect the behavior of the light in a larger beam than its geometrical cross-sectional area.

The anomalous diffraction theory of van de Hulst (1957) can also be used to calculate the scattering efficiency of particles with refractive index up to about twice that of the surrounding medium:

$$Q_{att} = 2 - \frac{4}{\rho} sin\alpha + \frac{4}{\rho^2}(1 - cos\alpha). \tag{1.7}$$

where $\rho = (4\pi a/\lambda)(m - 1)$, m being the refractive index of the particle relative to the medium, and a the radius of the particle.

The scattering properties of natural waters

Scattering by pure waters is of the density fluctuation type, and so varies markedly with wavelength. Experimentally, scattering is found to vary with $\lambda^{-4.32}$ rather than λ^{-4} as theoretically predicted. This is a result of the variation of the refractive index of water with wavelength. Pure sea water ($35 - 38^o/_{oo}$ salinity) scatters about 30% more intensely than pure water. Figure 1-10 (Table 1) lists values of the scattering coefficients for pure waters and pure sea waters at a number of locations and wavelengths, collected from different references. The scattering coefficients of natural waters are much higher than those of pure water. Even the lowest value (0.016 1/m) at 546 nm for water from 1000m deep is 10 times as high as the value for pure water at that wavelength. Coastal and semi-enclosed marine waters have higher values due to the presence of terrigenous particulate material plus phytoplankton.

One can see that most of the data was collected locally in various locations around the world, and is mainly empirical. There is no general theoretical way to calculate exactly what would be the scattering coefficient at a given area, not mentioning local events and time effects. Estimations and extrapolations based on the existing collected data, and knowledge of the expected water properties at the location should be applied, which affect the accuracy of the conclusions that can be derived from the data.

1.3.5 The upward flux and its measurement

A photometer in an ORSS pointing down at any shallow water body can receive light reflected by few different objects (Fig. 1-12):

- Reflection from bottom entities.
- Scattering and reflection from the water column.
- Reflection of skylight at the surface.
- Reflection of the direct solar beam.
- Scattering within the atmosphere.

Only the first of these five contains information about the underwater entities of interest. The effect of the water column on the signal is significant. The light leaving the water surface contains mixed information. Kirk refers to it as emergent flux. The essential problem is to quantify the emergent flux due to the water column in the presence of other light fluxes. This knowledge, together with characteristics of the light signature of the bodies of interest, will bring us closer to interpretation of the received signal.

Note: For deep ocean remote sensing applications, the emergent flux is the measured target itself, since it holds the information about the water column, or the water surface.

The photometer used to measure the light flux could in principle be either an irradiance meter, receiving light through an angle of 180^o with its cosine collector, or a radiance meter with a narrow angle of acceptance. In practice it is usually the latter, since the irradiance meter has the disadvantage of receiving all the upwelling light, including the reflected solar beam, and cannot be directed at a specific location. To avoid receiving the surface reflected solar beam, the radiance meter can be directed at a location well outside the solar glitter pattern.

A more difficult problem is how to account for the light originated by atmospheric scattering. About $80-90\%$ of the signal received by a satellite-borne meter originates in Rayleigh (air molecule) and aerosol (particle) scattering. Although the problem is less significant for low-flying aircrafts, we need to remember that the greatest interest for such a system is near the coast, were the water meet land, and the atmospheric properties are not stable. To some degree, there are models to predict and account for atmospheric effects, but this is not yet a completely solved problem.

Skylight also originates in atmospheric scattering, and the correction for it is lumped in with the total atmospheric scattering correction. An alternative procedure is to carry out the measurements at an angle of 53^o to the vertical. Light reflected from a plane surface at this angle (Brewster's angle) is polarized and can be eliminated by placing a polarizing filter over the radiance meter. However, as a consequence, the air mass through which the light travels will increase by a factor of 1.67, which can be a serious disadvantage.

1.4 Background Summary

I presented an available state-of-the-art hyperspectral imaging system that allows a spatial resolution of 1x1m and spectral resolution of 5.5 nm, with 72 bands to cover the visible spectrum. The amount of data recorded by such a system suggests that the practical problems of interpretation and analysis are way behind the available technology.

I presented one approach of many existing attempts to model the environment, so that the data could be analyzed. However these existing models are highly dependent on measured and empirical data from the location of interest.

The luxury of having this data does not always exist, specially when thinking about military applications, and quick response times.

By understanding the nature of the underwater light field, and all the history of the light path until it was read by the sensor, one can get a clearer picture about the true meaning of the signal that the sensor is measuring.

After being able to analyze the received signal, we should also be able to break this signal to its components and use classifying algorithms, considering also the averaging effects of the pixel size, so that useful conclusions can be maid. Since the classification can only be as good as the available spectral library, *in-situ* measurements of spectral properties of elements of interest should be collected. This may vary from natural bottom entities of the marine environment (such as sand, corals, vegetation, etc.) to specific elements of interest (such as mines, ship wrecks etc.).

This brings us to the need of *in-situ* measurements, which is the main area of concentration of my work. For *in-situ* measurements, one needs appropriate instrumentation. The next chapter is dedicated to such an instrument - the Benthic SpectroFluorometer (BSF).

1.5 Figures - chapter 1

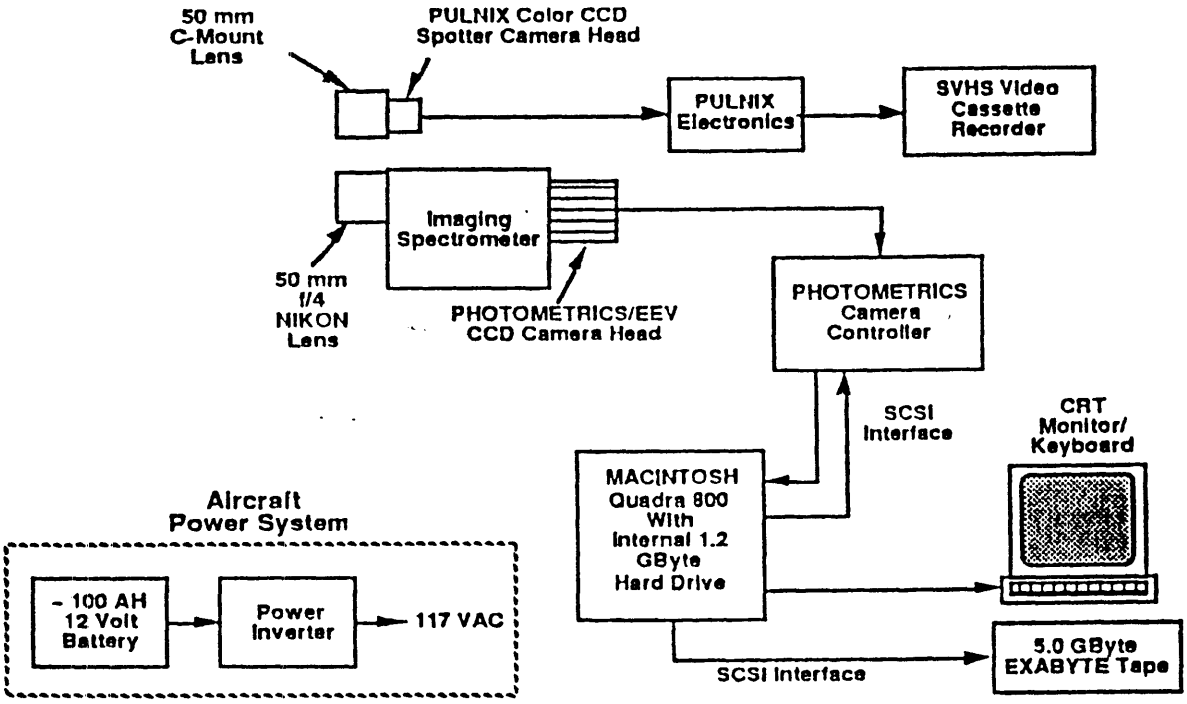

Figure 1-1: AAHIS sensor block diagram (SETS Technology, 1994).

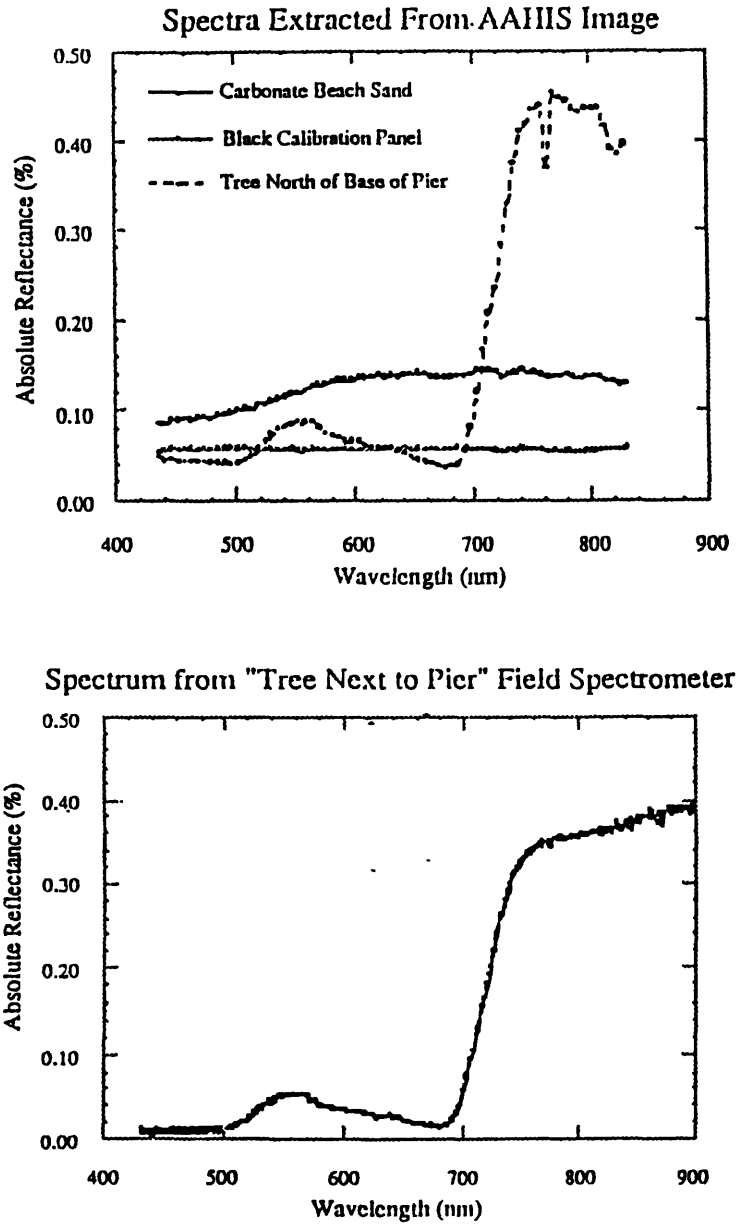

Figure 1-2: Derived AAHIS spectra vs. Field reading (SETS Technology, 1994).

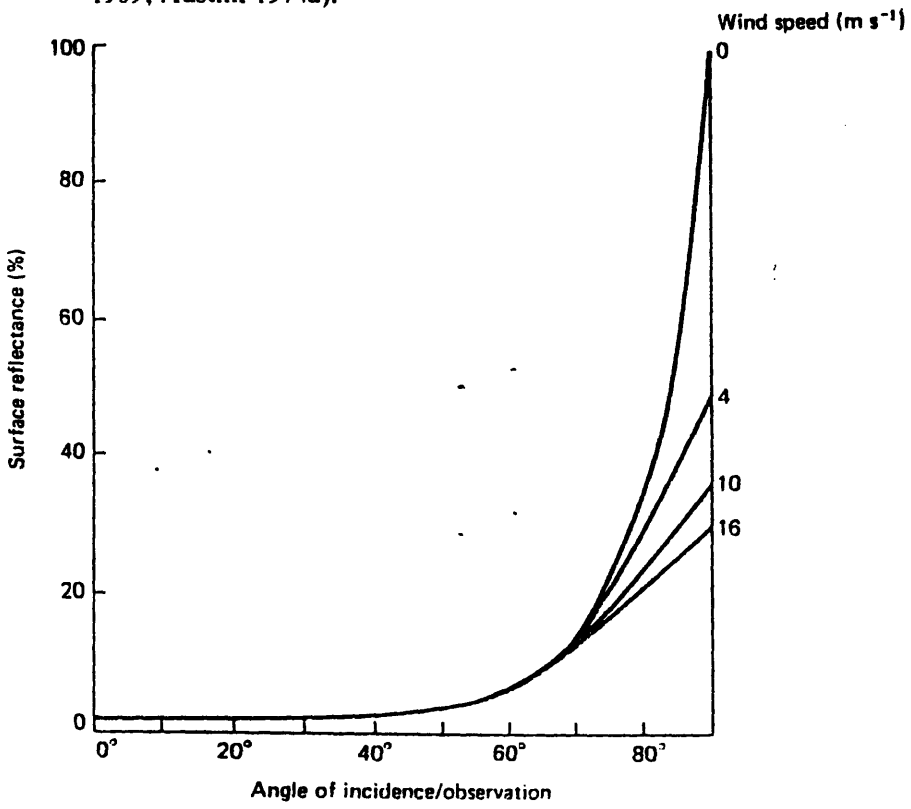

Figure 1-3: Reflectence of the water surface (Kirk, 1986).

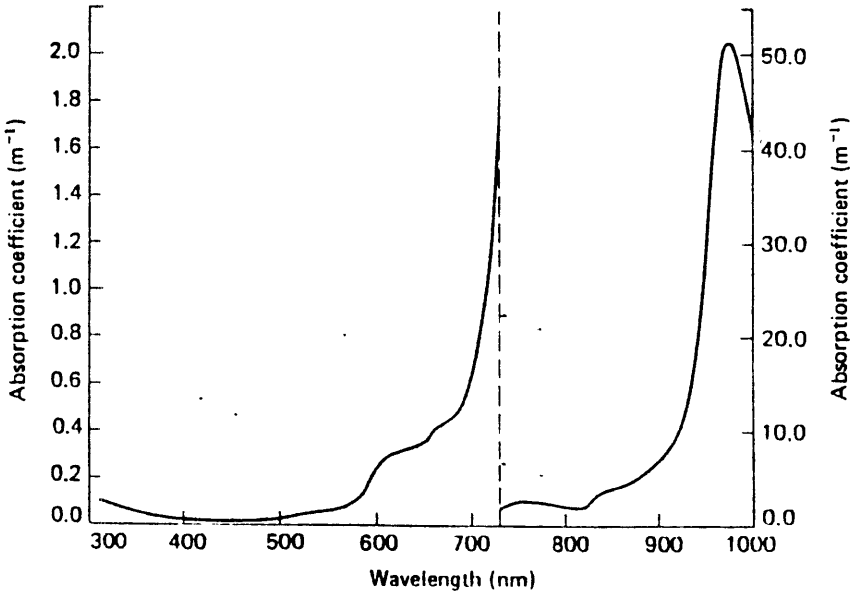

Figure 1-4: Absorption spectrum of pure water (Kirk, 1986).

Absorption spectra of soluble yellow material (gilvin) in various Australian natural waters (from Kirk, 1976*b*). The lowest curve (Batemans Bay, NSW) is for coastal sea water near the mouth of a river; the next curve (Clyde River, NSW) is for an estuary; the remainder are for inland water bodies in the southern tablelands of New South Wales/Australian Capital Territory. The ordinate scale corresponds to the true *in situ* absorption coefficient due to gilvin.

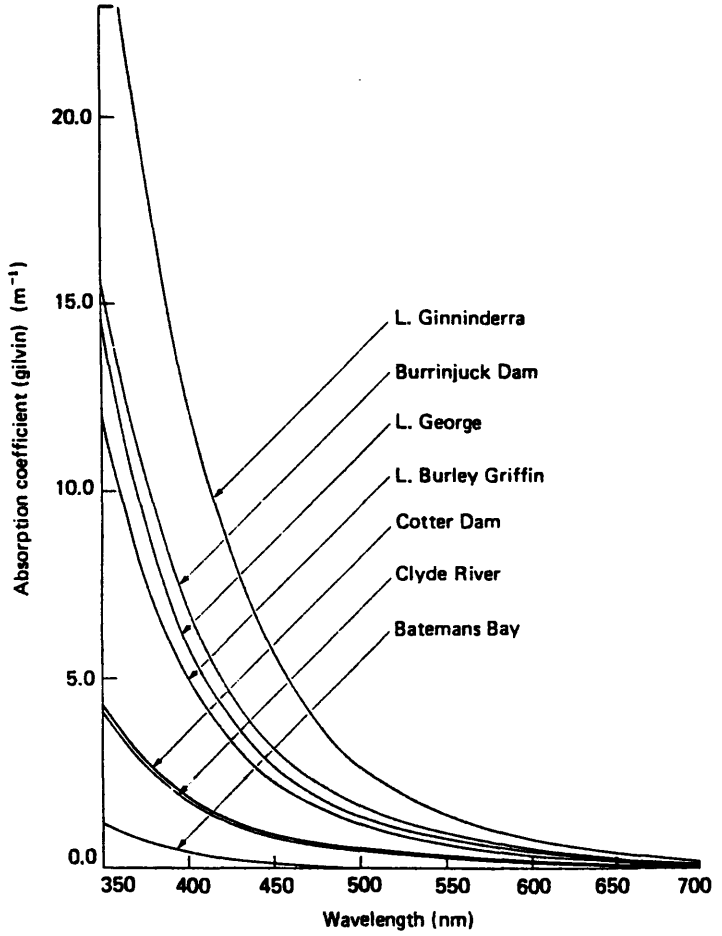

Figure 1-5: Absorption spectra of CDOM (gilvin) (Kirk, 1986)

Comparison of the spectral absorption properties of the different fractions in an estuarine water from southeast Australia – Lake King, Victoria (Kirk, unpublished data). Phytoplankton were present at a level corresponding to 3.6 mg chlorophyll *a* m^{-3} and the turbidity of the water was ~ 1.0 NTU.

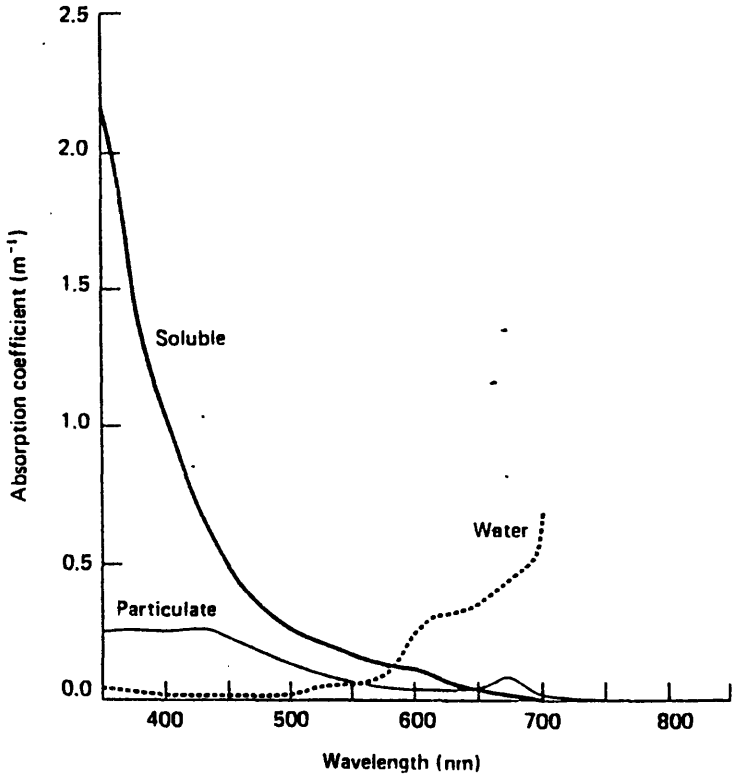

Figure 1-6: Spectral absorption properties of different fractions (Kirk, 1986).

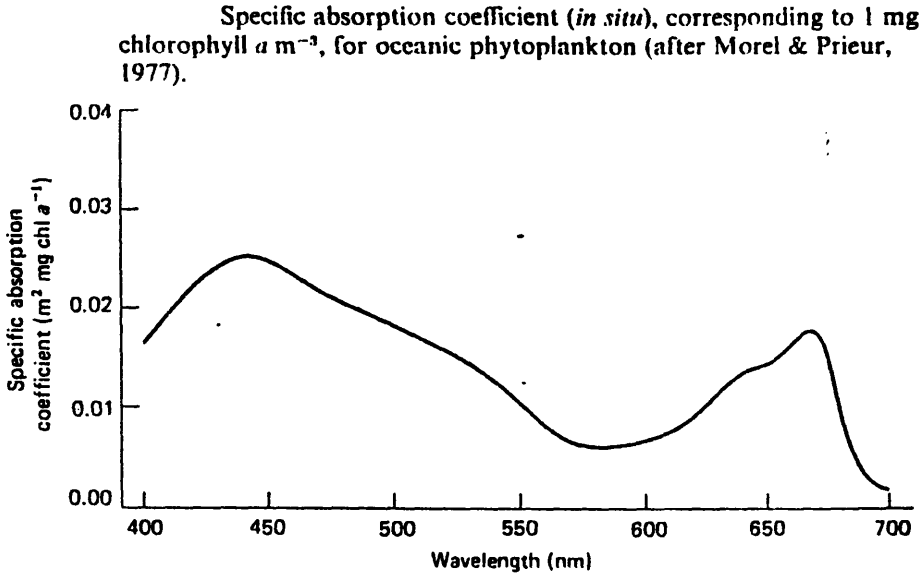

Figure 1-7: Phytoplankton specific absorption coefficients (Kirk, 1986).

Total absorption spectra of various natural waters in southeastern Australia (Kirk, 1981*a* and unpublished data). (*a*) Lake George, NSW. (*b*) Lake Burley Griffin, ACT. (*c*) Burrinjuck Dam, NSW. (*d*) Lake King, Victoria. (*e*) Jervis Bay, NSW. Waters *a*, *b* and *c* are inland, *d* is estuarine, *e* is marine (Tasman Sea). Chlorophyll and turbidity data for waters *a*–*d* are given in the legends to Figs 3.6 and 3.7. The Jervis Bay water (*e*) contained 0.2 mg phytoplankton chlorophyll *a* m^{-3} and was optically intermediate between Jerlov oceanic water types II and III.

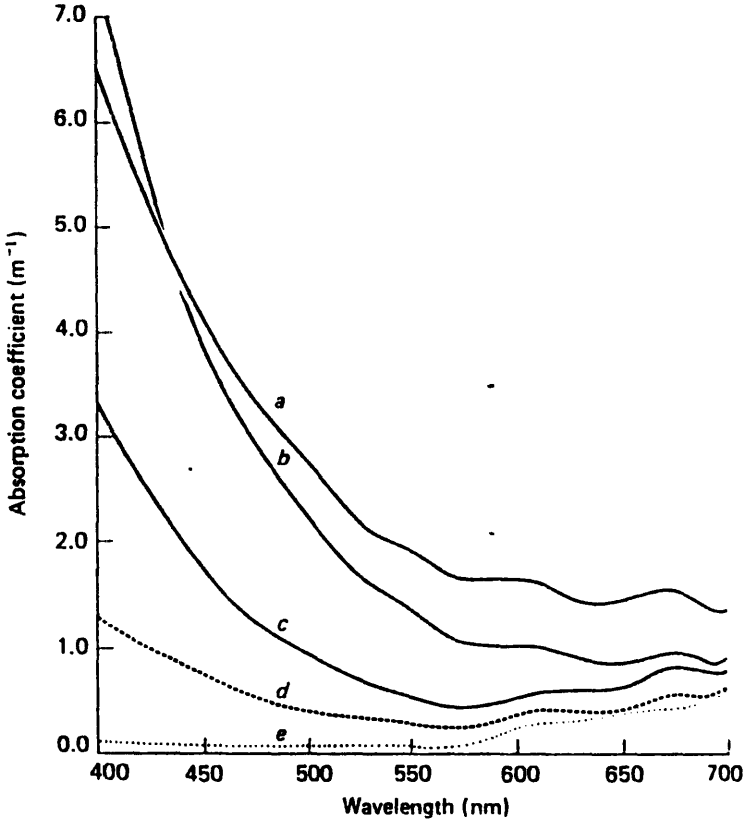

Figure 1-8: Total absorption spectra of various waters (Kirk, 1986).

Angular distribution of scattered intensity from transparent spheres calculated from Mie theory (Ashley & Cobb, 1958) or on the basis of transmission and reflection, or diffraction, transmission and reflection (Hodkinson & Greenleaves, 1963). The particles have a refractive index (relative to the surrounding medium) of 1.20, and have diameters 5–12 times the wavelength of the light. After Hodkinson & Greenleaves (1963).

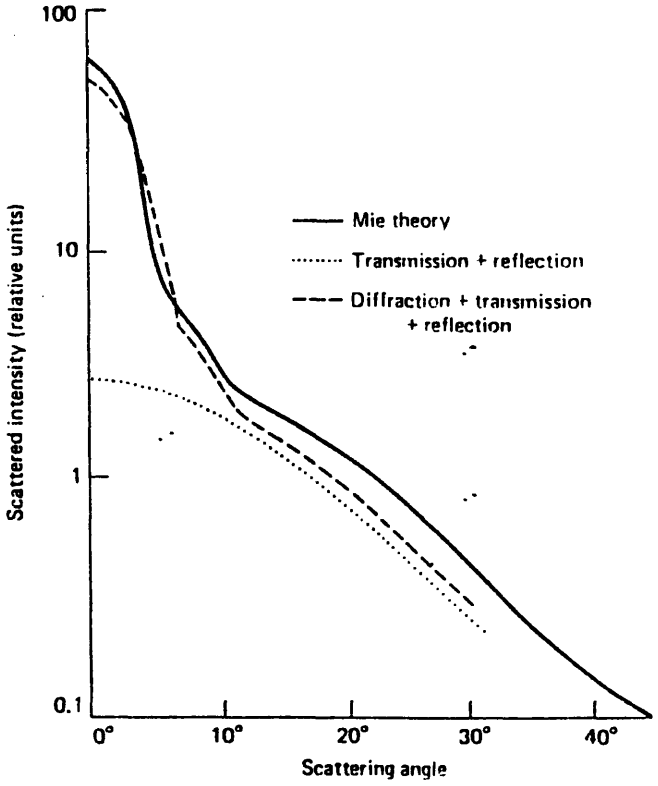

Figure 1-9: Angular distribution of scattered intensity (Kirk, 1986).

Water	Wavelength (nm)	Scattering coefficient, b (m^{-1})	Reference
Pure water	400	0.0058	327
	450	0.0035	327
	500	0.0022	327
	550	0.0015	327
	600	0.0011	327
Pure sea water	450	0.0045	327
	500	0.0019	327
Marine Waters			
Atlantic Ocean			
Sargasso Sea	633	0.023	275
	440	0.04	214
Caribbean Sea	655	0.06	214
3 oceanic stations	544	0.06–0.30	271
Bahama Islands	530	0.117	363
Mauritanian upwelling[a]	550	0.4–1.7	330
Mauritanian coastal[b]	550	0.9–3.7	330
Pacific Ocean			
Central (Equator)	440	0.05	214
Galapagos Islands	655	0.07	214
	440	0.08	214
126 oceanic stations (av.)	544	0.18	271
Offshore, South California	530	0.275	363
Kieta Bay (Solomon Is.)	544	0.54	271
Lagoon, Tarawa atoll (Gilbert Is.)	544	1.04	271
San Diego harbour (California)	530	1.21–1.82	363
Indian Ocean			
164 oceanic stations (av.)	544	0.18	271
Mediterranean Sea			
Tyrrhenian Sea (1000 m depth)	546	0.016	326
Western Mediterranean	655	0.04	188
Bay of Villefranche	546	0.1	326
Baltic Sea			
Kattegat	655	0.15	214
South Baltic	655	0.20	214
Bothnian Gulf	655	0.28	214
Black Sea			
33 stations (av.)	544	0.41	271
North Sea			
English Channel	546	0.65	326
Inland Waters			
USA			
Lake Pend Oreille[c]	480	0.29	376

Figure 1-10: Table 1: Scattering coefficients values for various waters (data from Kirk, 1986).

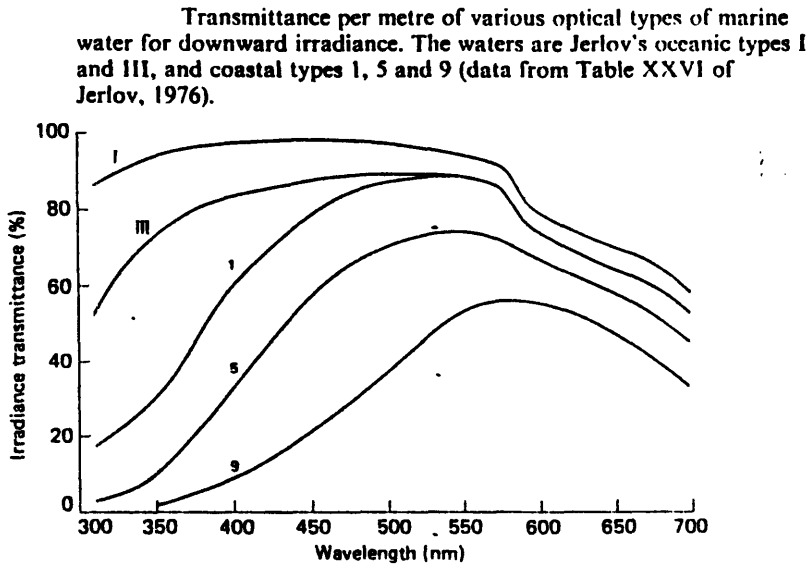

Figure 1-11: Jerlov's water classification (Kirk, 1986)

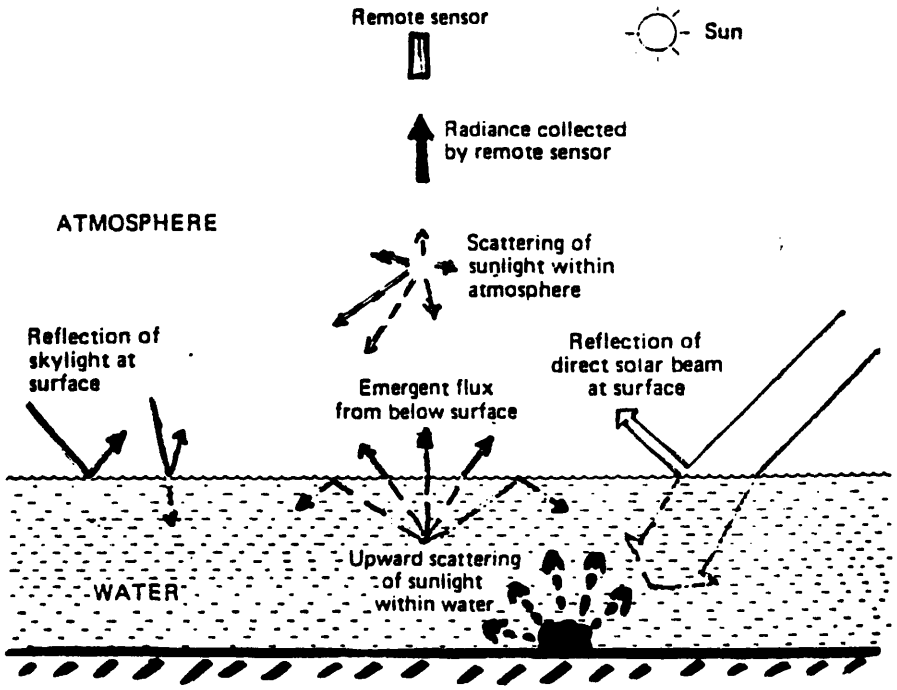

Figure 1-12: Different signal origins (Kirk, 1986)

Chapter 2

The Benthic SpectroFluorometer

2.1 Description of the BSF

The BSF was designed and built by Dr. Charles H. Mazel from the OE department in MIT. A major part of my work during the last year was to assist Dr. Mazel to improve, characterize and calibrate the instrument. Improvements were made in the operation and control of the instrument, as well as in performance and human interface.

Dr. Mazel's original interest was to study coral fluorescence, thus this instrument was designed to allow *in situ* measurements of corals optical response to projected light with controlled wavelength. However, the instrument is capable of operating in either passive or active mode, to measure optical properties of any surface. In fact the instrument measures the spectrum of any visible emission which the detector brings, through a fiber optic, to the CCD spectrometer. It is up to the operator to decide how to use it and what to do with the data.

Technical details:

The instrument is a sealed, self contained spectrometer unit with on-board computer and optics unit which are carried and controlled by a SCUBA diver, and can be operated under water. Since water attenuation does not allow sun light to penetrate deep into the ocean, the target operation depth of the BSF was relatively shallow (of the order of 60 - 100 ft). This was also the limitation imposed by normal diving operation. Thus, the instrument originally was designed and built for low pressure operation. It is more then likely that the instrument can stand higher pressure as well, but it had never been tested. The instrument was tested and fully operational at a depth of 60 ft of water.

The instrument is divided into few sub systems (Fig. 2-1):

The heart of the system is a *Tattletale* model 7 (TT7) computer board (by *Onset Computer Corporation*) connected to an *Ocean Optics* S1000 spectrometer board. This is a compact, PC board sized CCD spectrometer which covers the spectral range from approx. 300 nm to 760 nm. The spectrometer CCD array has 1100 elements

(pixels). By controlling the clock frequency, the computer controls the integration time at which the CCD elements count photons encounters. In this way the signal can be optimized to the amount of measured light for best SNR, while avoiding saturation.

The spectrometer performances are set by two parameter: the amount of light getting to the array, and the width of the light beam. These two parameter are specified by the diameter of the fiber optic, which brings the light into the spectrometer, and a slit in the beam path. The first controls the amount of light received, and the latter controls the resolution (or pixel separation).

A 600μ fiber optic and a 50μ slit were chosen for the desired resolution of about 5-10 nm, with the low signal levels expected during operation. (remember that the target signal levels expected for the instrument are relatively low, due to low fluorescence emission levels).

After installation, the fiber and slit are constants for the system, and can not be changed during operation. Changing one of these parameters will change the system characteristics, and requires new calibration.

After passing the 50μ slit, the light strikes a diffraction grating component which disperses it onto the CCD array, and separates the signal by its wavelength, such that the short wavelengths (UV) get to one side of the array (low number pixels), while the other end sees the red.

A 12 bit A/D converter chip converts the analog signal that comes from the S1000 to a digital signal that the TT7 can read.

The TT7 control the following sub systems:

- S1000

  Linear array spectrometer, by *Ocean Optics Inc.*

- 120MB hard disk

  To store collected data for post processing.

- A white light source

  A Metal Halide, 21W model M21E001 discharge lamp by *Welch Allyn.* This lamp was chosen due to its relative low power consumption, and the built-in elliptical reflector. The optical system is now being redesigned to correct for some of the problems that were found during operation with the *Welch Allyn* lamp, such as: electric shock to the system when firing the lamp, 20sec warm up time, dead spot in the middle of the light beam. The new system is expected to be operational this summer.

  In fluorescence mode the light from the lamp goes through interference filters that produce wavelength controlled emitted light. The filters can be switched by the operator during the dive (up to four different filters).

- 3" LCD display

  To allow visual output during the instrument operation.

- Key press input

  A magnetic switch that controls the instrument software flow.

- Alphanumeric "joy stick like" keypad

  To enter notes to the stored data file.

- Submerged speaker

  An audio output indicator for the diver.

- Pressure sensor

  To record the depth at which measurements were done.

All the above sub-systems are held in two standard *Ikelite* sealed housings, that were customized and modified for the instrument requirements. The system is powered by a 12V, 7.0 AH sealed rechargable battery (*Power Sonic* model PS1270) or the *Panasonic* CCR12V7.2P.

The system is separated into two independent housings, that are connected through a sealed hole in their side walls, as follow:

- Power and optics unit

  Contains the main battery, the light source unit and the light filters.

- Electronics unit

  Contains all the electronics, the LCD display, the speaker, the communication interface, the pressure sensor and the "joy stick" keypad.

In older model the light emitter was a liquid light guide that carried the light from the source in the power housing to a probe, held by the diver. The detector was a water proof fiber optic that carried the measured signal to the S1000 spectrometer in the electronic housing. Originally the emmitor and the detector were two independent cables, that were held in a 45^o angle by a specially designed probe head. However, to improve performances, a new configuration was designed. The new configuration is a single 600μ fiber optic (for the detector), surrounded by three rings of fiber optics bundle (as an emmitor). A bifurcated cable holds the fibers together at the desired geometry, and separates into two cables at the entrance to the instrument. A magnetic switch, placed on the handle of the probe, controls the program flow by a single press operation, and menu options that are displayed on the LCD display. The operator can view the instrument OS flow on the display, choose different software instructions, or view in real time the results of individual scans.

There are two more boards connected to the system in the electronics housing. A general purpose customized board, where the developer can add his own functions to the system. This board is supplied with the TT7, and it is connected to the TT7 pins. The other board is a self made board that holds all the connectors to the auxiliary devices such as speaker, key press, joy stick etc. All those connectors are color coded.

The operator can decide which of the data scans should be stored on the 120 MB hard disk as an ascii file. He can also enter his own notes to the file header. Each file is given a name, based on the date and time of the measurement (time stamp).

Operating System Software:

The TT7 has a built-in communication capability. During development mode, the TT7 can be operated through a simple RS232 connection from an auxiliary PC, as a remote terminal. The development environment is either Macintosh or MS-DOS. In our case, we used a Macintosh Powerbook 520 as the auxiliary platform, Think C, Cross-cut (a customized communication package supplied by *Onset computers*) and White Knight as software tools, and simple RS232 cable connected to the Mac Modem port for communication.

A standard ANSI C code was developed and compiled on the Mac. The executable code was then loaded to the TT7 first 256 memory KB, which are available for programming (thus, this is the code size limitation). There are two more memory MB (called pseudo memory) on the TT7 cheap. These are available for variables storage during run, and should be controlled by the programmer. The access to the pseudo memory is done directly by address, and not through standard C arrays and matrices commands, thus demanding careful attention and control while programming and using this memory space.

After the code development has finished, the executable file can be loaded to the TT7 EEPROM, where it is kept in the memory. An auto start mode can be invoked for the operation phase, so the code will start running automatically with every POWER ON cycle.

The operator can navigate in the software by pressing a magnetic switch (key press) that is connected to one of the TT7 TPU pins. This pin voltage is monitored by the TT7, so the programmer can use a "press event" as an action mark in the code. The user can follow a visual output on the 3" LCD display and an audio output from a submerged speaker, to allow software flow control.

A submerged ON/OFF switch was added to the system, to allow the diver to cycle the power underwater.

The BSF is undergoing constant development and improvements. The main motivation for current changes are two:

1. Addressing problems that were found in former use of the instrument (such as optical performances, cracks in the housings).

2. Minimizing the reasons for the instrument to be opened during field operation.

Issues that are currently in progress:

- Optical "through the housing" communication set up.

- Re-engineering of the optical unit.
- Re-packaging the instrument is a single housing.
- Improving electronic components.

All the above are expected to be finished before the planned field trips, this summer.

2.2 Dark current correction

Every scan of the BSF produces an output reading of 1100 numbers, corresponding to the 1100 elements of the CCD. I refer to this output as a curve, although it is actually 1100 discrete values, covering the BSF spectrum. This reading however, holds also the inherent dark current noise produced by the spectrometer.

What is dark current noise?

The dark current noise (thermal noise) is caused by the random motion of carriers in a conductor. If we were to measure the voltage of a simple resistor R, remembering that the electrons kinetic energy in a conductor is proportional to its V^2, we would find that

$$V_{RMS} = \sqrt{4KTR\Delta f} \tag{2.1}$$

where Δf is the frequency band width of the measurement, K is Boltzman's constant and T is temperature. In our case, Δf is the s1000 sampling frequency which is constant, and T is relatively constant as well. However, by allowing long integration time, we allow a buildup of voltage in the CCD elements, which results is higher noise (higher dark current).

The above is the reason for cooling sensitive detectors (such as Photomultipliers) to a very low temperature (around 77^oK), to minimize the dark current noise.

When the instrument detector is pointing at a complete darkness, we would like the spectrometer to read zero (no light getting to the CCD array). However, the actual reading that one gets in such a case is not zero. This reading is the dark current noise. This noise needs to be subtracted from the data to get the real signal of the measurement.

The dark current noise depends on the scan integration time (or clock frequency which is controlled by the on-board computer). The longer the CCD is waiting to collect photons, the higher the noise is. The dark current readings were found not to be consistent. There were cases where two different readings with the same clock frequency did not produce the same dark current curve (differences of up to 20% were found). Our assumption is that this has to do with the instrument warm-up time, but in general this issue should be further investigated. As a result of this inconsistency, we use the instrument to get spectral shapes curves rather than measuring absolute radiometric values. The instrument is also capable of relative measurements, as long as the readings are done close to each other in time.

The method that was originally used to compensate for the dark current noise was as follows: for each sample reading, an additional reading was taken, with the detector face covered. The dark reading was taken with the same clock frequency as the sample, to maintain the same integration time. This dark current reading was then either saved on the disk for post processing dark current correction, or subtracted from the sample data before saving. This process was time and disk space consuming. The operational difficulties and risks of operator errors suggested that

an improvement to the excising procedure is needed.

After characterizing the instrument in the lab, two properties of the dark current response were found.

- The general shape of the curve always repeat itself. This has to do with the general sensitivity of the CCD array, however it will vary in magnitude, according to the clock frequency.
- The sensitivity of the 1100 array pixels remains constant relative to one another. This relationship creates a typical pattern to the curve that would vary in magnitude with respect to the frequency, but would keep the relative value of the pixels. i.e. if pixel n reads 98% of the average curve value, it will stay 98%, even when the value of the average is changing with the frequency.

From this two rules we can learn that if we are able to tell what the magnitude of a dark current reading curve would be, and a typical dark current prototype exist, the curve can be predicted. Once the dark current curve is predicted, there is no need to scan each time to get the dark current noise.

2.2.1 Dark current characteristics

Curve Shape

About 300 dark current scans were taken with two S1000 spectrometers. In general it was found that each spectrometer has its own dark current "signature". This signature is a typical dark current curve shape. The shape of the curve remains the same at all frequencies, but the magnitude of the curve changes with integration time. The longer the integration time (the lower the clock frequency), the higher the dark current value. Please refer to Fig. 2-2.

However, it was also found that the spectrometers are not repetitive, and may read different values at each reading session (Fig. 2-3). Nevertheless the shape of the curves remains the same.

Pixel pattern

Looking closely at Fig. 2-3 one can see that the pixels form a repetitive and constant pattern, that is unique for each pixel. Normally, each pixel reading is the result of how many photon encounters a single element of the 1100 CCD array in the spectrometer is counting within the integration time.

While considering dark current measurements, no light is getting to the detector, thus ideally the reading should have been zero. The non-zero dark current reading does not come from photons reaching the diode, but from inherent electronic noise. However, each element has its own sensitivity with respect to its neighbors, thus has a different dark current value. The relative sensitivity is constant, thus the pixels form a pattern that is repetitive, and unique. Each diode has its own unique dark current "signature".

Ambient Light

Relative to the signal levels that we are measuring, normal solar radiation does not produce much short wavelength UV light (less than about 350nm), as can be seen from Fig. 2-4 (the UV range less than 350nm corresponds to pixels 0 to about 180).

Fig. 2-4 is composed of two curves:

- Normal solar radiation.
- Dark current curve, taken with the same integration time, shortly after the first curve was taken.

It can be seen that the curves coincide in the pixel range less than about 180. This means that the only readings at these pixels are due to dark current noise, and that no "real" light gets to the array at these pixels.

Based upon this fact, we assume that we can use the values of the pixels less than 180 for dark current prediction.

2.2.2 Dark current prediction

Data preparation

The previous section suggests that we need three pieces of information in order to predict the dark current curve for the full spectrum, at any given clock frequency:

- The magnitude (offset) of the dark current curve.
- A way to predict the magnitude of the pattern.
- A prototype pixels pattern, unique for each spectrometer.

The starting value of the curve

As shown in the previous section, the pixels range less than 180, is "clean" of measured light, and thus can be used for dark current prediction. To be on the safe side, I have only used the pixels 40 to 140 (less than about 320nm), to avoid any influence from true existing light.

Three sets of dark current measurements were taken at three different times. Each set had 6 - 10 different readings covering the relevant frequency range (2 - 100 KHz). Each reading was an average of 5 different scans, taken immediately one after the other. The mean value of pixels 40:140 was calculated for each reading (Column M1(40:140) in Fig. 2-5). This value will be the same for a dark current measurement (no incoming light) and a sample reading (where a incoming solar light is measured). This value will tell us the offset (starting value) of the dark current curve.

The magnitude of the pattern

The standard deviation was calculated, for the same range of pixels (Column std(40:140) in Fig. 2-5). The values of the standard deviation show the magnitude of the pixels pattern, with respect to the mean value of the curve (M1).

Plotting STD vs. M1 showed an almost linear relationship between these two (Fig. 2-6). This is the characteristic behavior of the spectrometer. Based on this relationship, one can predict the magnitude of the pixels pattern, if the value of M1 is known.

Pixel pattern prototype

A prototype pixel pattern can theoretically be taken at any integration time. However, to maximize SNR, a low frequency (2KHz) measurement (and thus, a long integration time which produces a high dark current reading) was chosen to serve as a prototype file. The value of M1 was subtracted from the dark current reading, to produce a curve that holds the pixel pattern, but is centered around zero for pixels 40:140. (In other words, the mean of pixels 40:140 in the prototype file is zero). These values were saved into an ascii file, and copied onto the instrument hard disk. I will call this array "SIGMA" for future reference.

For future use, calculate the value of STD for pixels 40:140. This value will be used later to calculate a scaling factor for the pixels pattern. Lets call this value STD_REF.

2.2.3 Prediction Algorithm

Concept

Say we performed a reading and we have an array of 1100 numbers, corresponding to 1100 pixels. Lets calculate M1 of this sample (mean of pixels 40:140), and call it M1_SAM. We already know that this M1_SAM, which was calculated with true light getting to the sensor, is the same as what M1 would have been for a dark current reading when no light gets to the detector, with the same clock frequency. Now, from the linear curve (Fig. 2-6), get the expected STD for this M1. Call this value STD_SAM. Calculate the scaling factor for the pixel pattern values:

$$FACTOR = STD\_SAM/STD\_REF. \tag{2.2}$$

Finally, to build the full predicted dark current curve, use:

$$DARK(i) = M1\_SAM + FACTOR * SIGMA(i). \tag{2.3}$$

Prediction Recipe

After all the preparations, the actual prediction is simple, and can be done in a "cook book" manner:

1. Get a data scan, at any clock frequency.
2. Calculate the mean of pixels 40:140 (get M1_SAM).
3. Calculate the STD_SAM for the pixels pattern (Fig. 2-6).
4. Calculate FACTOR = STD_SAM / STD_REF.
5. Multiply the values of the SIGMA by the scaling factor (FACTOR).
6. Add the results to M1 to get a predicted dark current curve (Eq. 2.3).

2.2.4 Results

Tests were made in a frequency range from 4KHz to 60KHz. In all cases dark current curves were both calculated (using the above described algorithm), and directly measured by covering the detector. The results show a successful prediction. The prediction accuracy decreases with higher frequencies, but the dark current value is smaller when the frequency is higher, thus the total result is a good dark current prediction (within 2% of the real values).

The benefit of a good dark current correction is demonstrated in Fig. 2-7. The original vs. corrected data (using the prediction algorithm) is plotted, showing a significant improvement after correction.

2.3 Wavelength calibration

The product of a BSF scan is an array of 1100 numbers, representing voltages produced by the 1100 elements of the CCD array in the S1000. The voltage measured is translated to integer numbers by a 12 bits conversion, controlled by the A/D card.

The value of each element represents the number of photons that a specific element had seen during the scan integration time, and represent the amount of light at a specific wavelength. The wavelength distribution is controlled by a grating which disperse the light according to its wavelength, subjected to the system characteristics and sensitivity.

A calibration process is required to find the wavelength each element (pixel) is reading.

Each spectrometer received from the company comes with a specification sheet which defines a second-order polynomial fit for the wavelength calibration.

In order to verify the accuracy of the company's calibration procedure, and also to get proficiency in the calibration process, we developed our own calibration process, and reached the expected conclusion - the company results are reliable, and can be used within the system resolution that we are working in.

2.3.1 Calibration procedure

A standard Mercury Argon (HgAr) Model HG-1 by *Ocean Optics, Inc.* lamp was used for calibration. This lamp produces a well defined and known emission peaks (Fig. 2-8), that can be referred to as known wavelength reference points.

An adjustable adapter for the detector was built to serve four purposes:

1. Hold the BSF detector in line with respect to the lamp output slit.
2. Allow adjusting the distance between the detector and the lamp, to avoid saturation.
3. Prevent ambient light from reaching the detector, adding noise to the measurements.
4. Help distribute the heat which was created by the lamp during the calibration process.

The scanning frequency was adjusted for a maximum SNR, and scans were taken. This scans produced a series of emission peaks, distributed across the pixels range. The results were plotted as a pixels vs. peaks graph (Fig. 2-9).

The next step was to identify a correlation between the measured peaks, and the expected HgAr emission peaks, remembering that second-order-effect peaks might add "imaginary" peaks to the curve. Having the factory calibration polynomial came handy, and helped identifying the relative emission peaks.

2.3.2 Sub-pixel precision

After identifying the relevant emission peaks, we needed to choose what pixel number to assign for them. Two options were considered:

- Choosing the pixel that measured the maximum voltage at the vicinity of the peak.
- Calculating an "average weight point" of the peak vicinity, using sub-pixel precision.

We chose the second approach, since we believed it to produce a more accurate result that takes into account the energy distributed on all the pixels that builds the peak. The S1000 resolution (5-10 nm) suggests that this approach is more adequate.

To find the sub-pixel value of a peak, a numerical integration was done to calculate the centroid of the curve:

$$C_s = \frac{\int R_\epsilon d\epsilon}{\int R d\epsilon} \simeq \frac{\sum R_\epsilon \epsilon}{\sum R_\epsilon}. \tag{2.4}$$

where (please refer to Fig. 2-10):

ϵ = Pixel number.

R_ϵ = Voltage count of pixel number ϵ.

$d\epsilon$ = Increment between pixels (=1).

Only pixels that measured more than 10% of the local maximum at the vicinity of the peak were considered, to avoid noise.

Please refer to 2-11 for an example of the results of the centroid calculations.

2.3.3 Sub-Pixel to Wavelength curve fit

Two approaches where checked, to find a function which will fit the sub-pixel numbers, and the actual emission wavelength:

- MATLAB POLYFIT function: finds the coefficients of a polynomial p(x) of degree n that fits the data, p(x(i)) = y(i), in a least-squares sense.
- Chebyshev polynomials and least square error method.

The reasons for choosing these two methods were the ease and availability of the use of MATLAB, and accuracy of Chebyshev polynomials in curve fitting.

Chebyshev polynomials

Chebyshev polynomials are defined as:

$$P(x) = \sum_{i=0}^{n} a_i T_i(x) \tag{2.5}$$

Where:

$T_o = 1.$

$T_1 = x.$

$T_2 = 2x^2 - 1.$

$T_3 = 4x^3 - 3x.$

$T_4 = 8x^4 - 8x^2 + 1.$

$T_5 = 16x^5 - 20x^3 + 5x.$

.

.

.

while $-1 < x < 1$.

Least square best fit

For a given set of n data points, let:

y_i = True value.

$P(x_i)$ = Predicted value by the polynomial.

$Err(a_o, ..., a_{n-1})$ = The difference (error) between y_i and $P(x_i)$.

A least square error definition for Chebyshev polynomials:

$$Err = \sum_{i=0}^{n} [y_i - P(x_i)]^2 = \sum_{i=0}^{n} [y_i - \sum_{j=0}^{n-1} a_j T_j(x_i)]^2. \tag{2.6}$$

Our goal is to choose a_j such that this error would be minimum. To get the coefficients, take the partial derivative of the error with respect to a_i, which will yield a system of n equations with $a_o, a_1, ..., a_{n-1}$ unknowns:

$$\frac{\partial Err}{\partial a_o} = 0. \tag{2.7}$$

.

.

.

$$\frac{\partial Err}{\partial a_{n-1}} = 0. \tag{2.8}$$

Implementation

In our case we have an array of 1100 integers in the range 1 to 1100. We need to convert them to the range of existence of the Chebyshev polynomials ($-1 < x < 1$):

$$x = -1 + \frac{2}{1100} * \epsilon. \tag{2.9}$$

After using the above two methods for comutations and comparing the results, I found that for two digits precision the results are identical. Thus, since the Chebyshev method is complicated compared to the MATLAB function POLYFIT, I continued to use MATLAB as my calculation tool.

2.3.4 Results

High order polynomials sometimes "misbehave" between the given data points. To control the quality of the ploynomial fit, one should either have data samples to cover all the needed range, or he can expect the fit to fail in extrapolation. I made the same calculations using 2nd,3rd,...,5th order polynomials, and compared the results (Fig. 2-12). One can see that the 5th order polynomial fit, although very good in the vicinity of the data points, doesn't look reasonable beyond the last point (greater than pixel number 650).

The 2nd, 3rd and 4th order polynomial curves look good, and the factory 2nd order calibration polynomial look just as good, if not better. A numerical comparison reveled small and insignificant differences between the polynomials. One can only count on his intuition when judging the behavior of the curves beyond the range of the data points, thus the 5th order polynomial was rejected, and the 2nd order polynomial fit was chosen as satisfactory.

As an additional test, I have applied the factory 2nd order polynomial on the sub-pixels results that I got. The results were within 2nm from the results given by the MATLAB 2nd order polynomial.

These facts allow us to use the factory calibration 2nd order polynomial, knowing that it is reliable and accurate enough for our purposes.

2.4 Spectral sensitivity calibration

Each spectrometer has its own sensitivity curve, and the BSF is not different. Although we are not using the BSF for absolute radiometric measurements, we can still correct for its internal sensitivity. The procedure is very simple: measure a well known signal, and compare your results with the expected signal. Dividing the two will yield the sensitivity curve for the instrument. The output of such a process is a correction curve, that each reading should be multiplied with, in order to account for the internal sensitivity of the BSF.

As a standard source we used a 45w quartz-halogen tungsten coiled filament lamp (Serial n. L-653) of Spectral Irradiance (OL 245A) by *OPTRONIC laboratories, Inc.* (Ref. [11]). This lamp was supplied with calibration data from the manufacturer, and a specific procedure for measuring it. The light is to be measured from a distance of 50cm, operated at 6.50 amperes DC. The importance of following the procedure is greater if one is trying to calibrate the instrument for absolute radiation measurements. In our case, we were only trying to measure the color temperature of the source, thus accuracy in following the exact set-up was less important. Nevertheless, an attempt was made to follow the procedure to the letter, especially keeping a stable current of 6.50 amps.

The data supplied by *OPTRONIC* does not cover all the spectral range of interest, but rather made of few discrete data points of selected wavelengths. Thus an adjustment process was needed for the continuous spectrum.

Using Planck's equation for black body radiation:

$$M(\lambda) = \frac{C1}{\lambda^5}\left[e^{\left(\frac{C2}{\lambda T}\right)} - 1\right]^{-1} \tag{2.10}$$

where

T Temperature in ^oK.

λ Wavelength in M.

$C1$ Constant $= 3.74 * 10^{-12} w/cm^2$.

$C2$ Constant $= 1.439 cm^oK$

It was found that the color temperature of the source is 2870^oK (Please refer to Fig. 2-13), which produced a well defined curve, covering the spectral range of interest (350-750 nm). Now, I measured the source with the BSF. (Fig. 2-14). Due to the CCD spectral sensitivity, the measured curve is different than the expected black body shaped curve (ignoring dark current noise). This means that a correction factor should be applied to every BSF measurement, where the specific shape of the radiation curve is of interest.

This correction factor is simply found by dividing the two curves of Fig. 2-14. The result is presented in Fig. 2-15, which is the spectral radiation correction curve for the BSF.

2.5 Future improvements

The BSF performance was compared with a well known and proven commercial spectrometer (PRR 600). The comparison was done by measuring the same scene (sand bottom in 10m depth of clear sea water),with both instruments, at about the same time, and comparing the results after normalizing the reading to match at one wavelength. As can be seen in Fig. 2-16, the results show good agreement between the two instruments. This build up confidence to use the BSF as a work tool, keeping in mind that still there are things that can be improved.

In addition to all the improvements that will be done to the instrument during the next few weeks, before summer of 1996 (which were mentioned earlier), there are more issues that need to be addressed, such as:

- Looking into absolute radiometric measurements.
- Understanding what causes the dark current inconsistency.
- Designing a better diver-instrument interaction method (for example: full keyboard capability).
- Upgrading electronics and hard disk for better performances.
- Re-engineering the optical unit, while considering the use of lasers as a light source.
- Looking into non-human carrying platforms (AUV for example).

All the above imply that there is plenty of research and design work that can and should be done on the instrumentation part of the project. Nevertheless, as it is, we have a very useful instrument that can be used for *in situ* measurements in its current configuration.

In the next section I present one topic, for which the instrument can be used: spectral measurements of coral samples, that are known to have fluorescence characteristics. This topic is only one step in the long way to the end goal of remote sensing of shallow waters in general and tropical reefs.

2.6 Figures - chapter 2

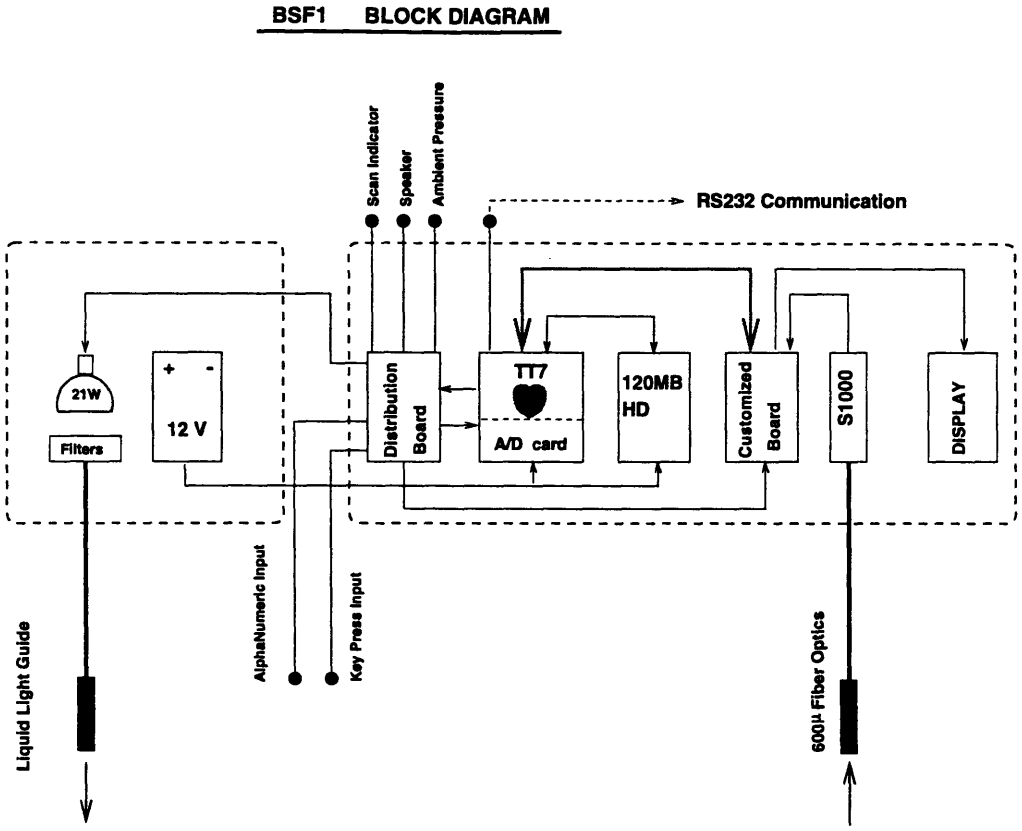

Figure 2-1: BSF1 - Block Diagram.

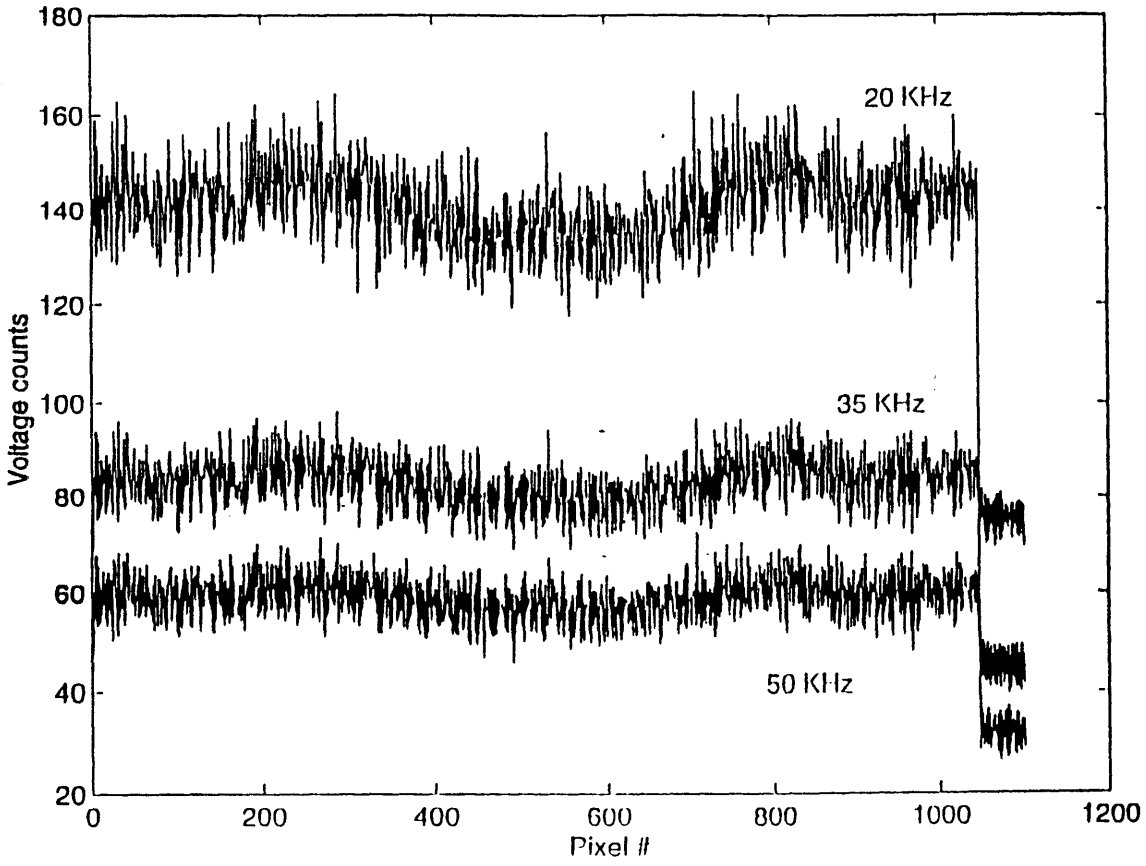

Figure 2-2: Dark current shape, different clock frequencies.

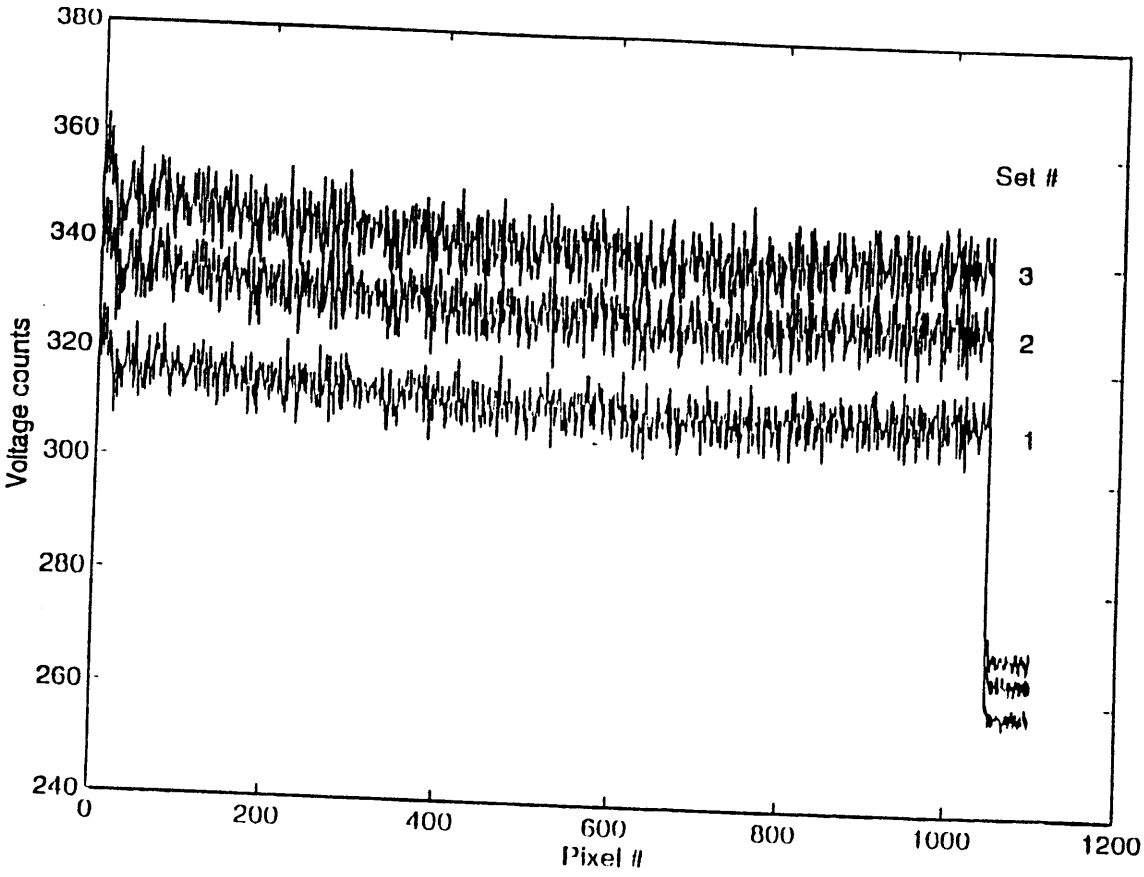

Figure 2-3: Dark current variability (Three data sets, 20 kHz).

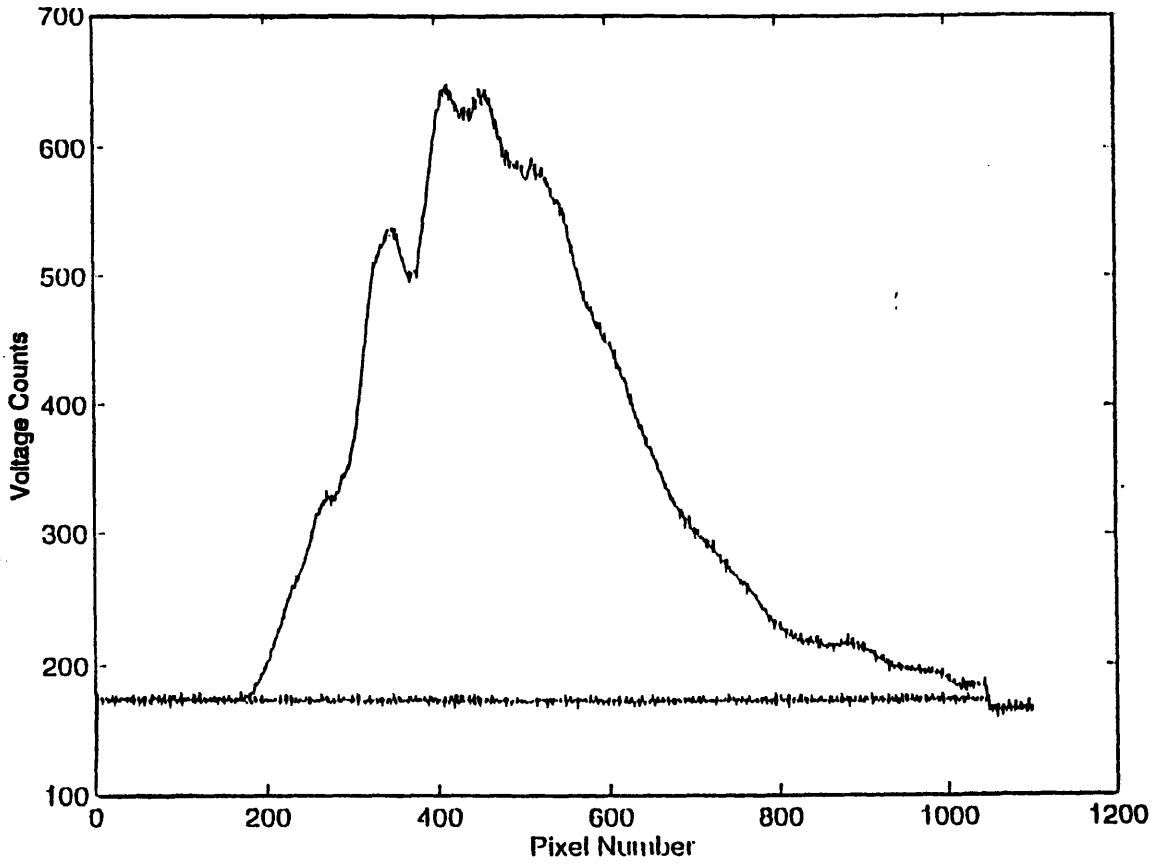

Figure 2-4: Ambient light and dark current readings (70 kHz).

DATA SET # 1 - 3/28/95

Freq.	M1 (40:140)	std(40:140)
2	1.4050e+003	34.9446
4	718.5307	18.3799
6	485.3020	12.4353
10	296.1881	7.6087
20	152.6465	3.8589
35	90.0901	2.3045
50	67.1416	1.8311
75	45.2624	1.4594
100	34.4604	1.2668

DATA SET # 2 - 3/28/95

Freq.	M1 (40:140)	std(40:140)
2	928.8267	23.1289
3	673.8040	17.0283
4	534.4842	13.5376
6	375.8416	9.4424
10	237.0040	5.8817
20	127.2040	3.1666
35	78.1267	1.9715
50	57.9178	1.6025
75	40.9485	1.3175
100	32.8050	1.2481

DATA SET # 3 - 3/28/95

Freq.	M1 (40:140)	std(40:140)
2	1.1607e+003	28.7166
5	514.7168	12.9584
9	296.4604	7.5218
15	184.8158	4.6217
20	144.0178	3.5732
30	97.3149	2.5003
50	62.0535	1.8400
60	52.2941	1.5267
75	42.4921	1.3906
100	33.3812	1.2606

Figure 2-5: Tabel I: Collected data from three data sets.

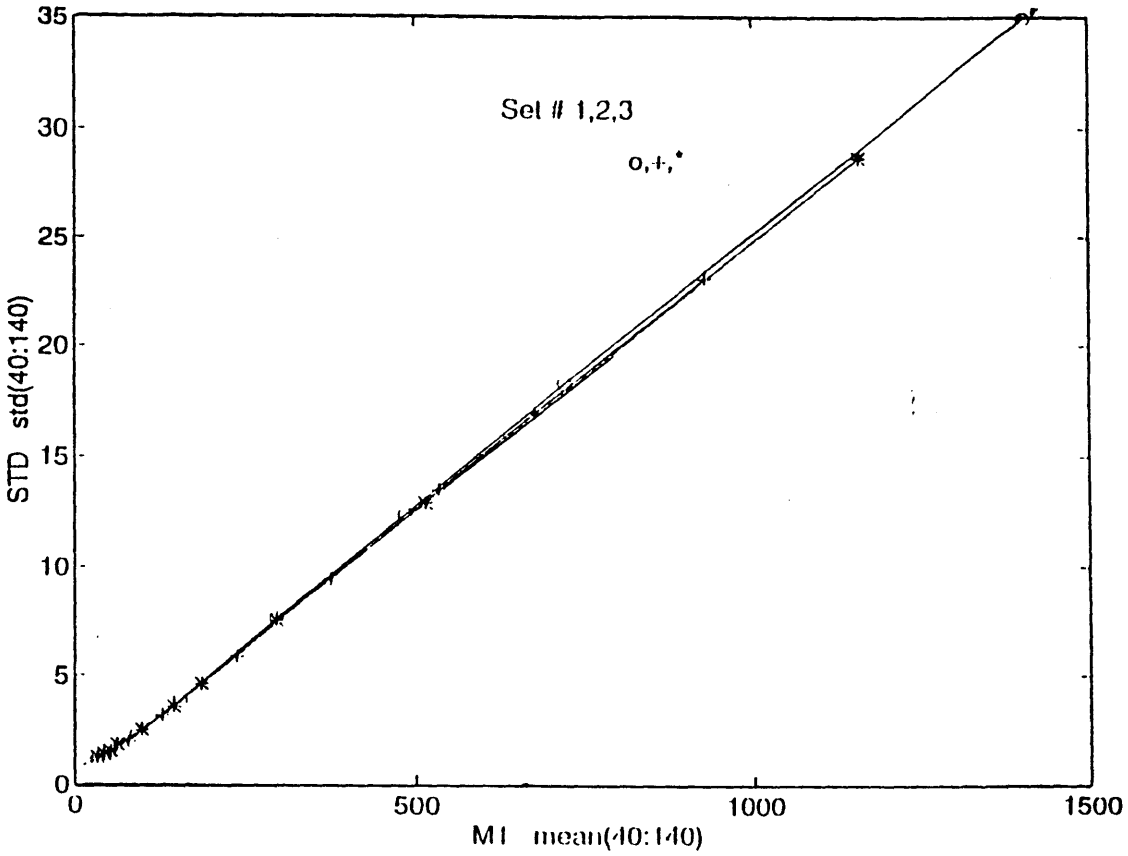

Figure 2-6: Linear relationship between M1 and STD (40:140).

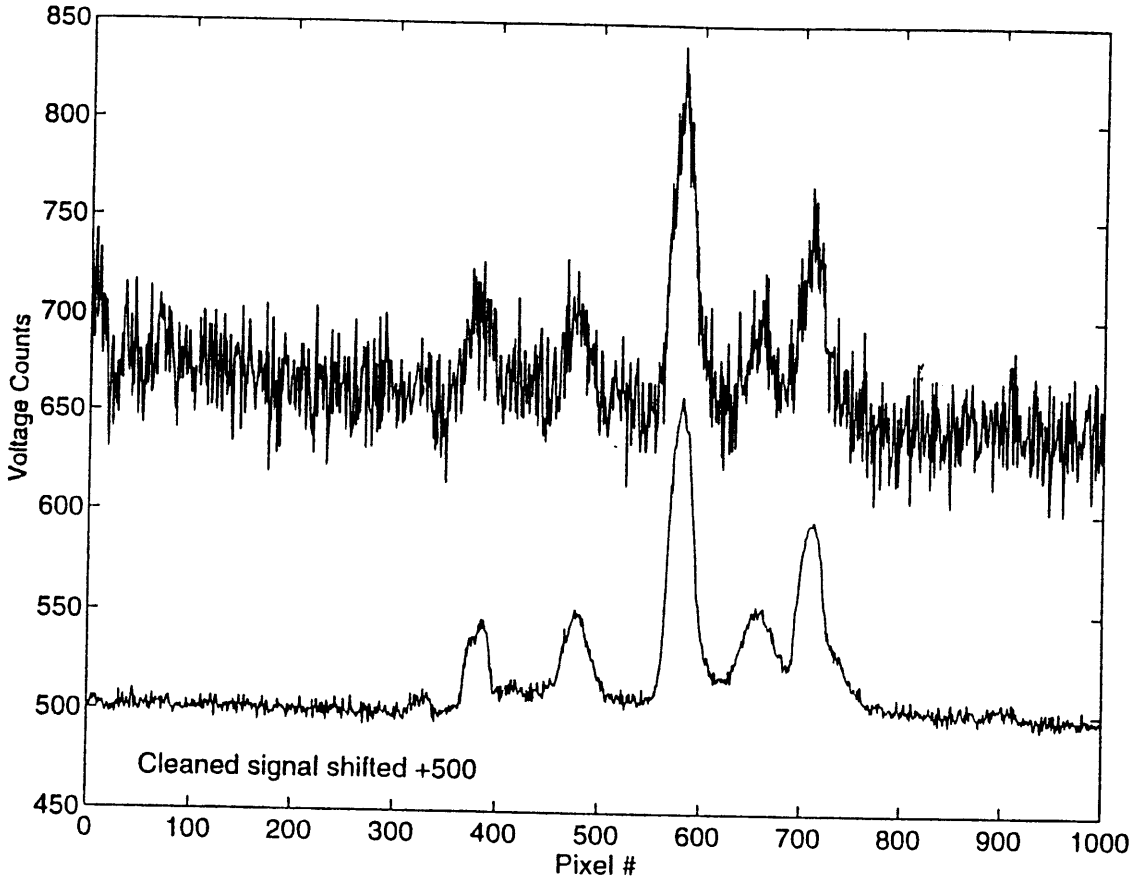

Figure 2-7: Original and corrected signals (Weak signal, 4kHz).

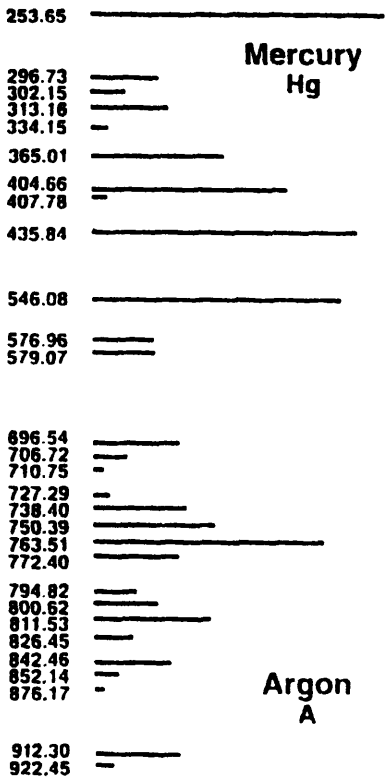

Figure 2-8: Standard Mercury-Argon calibration emission peaks

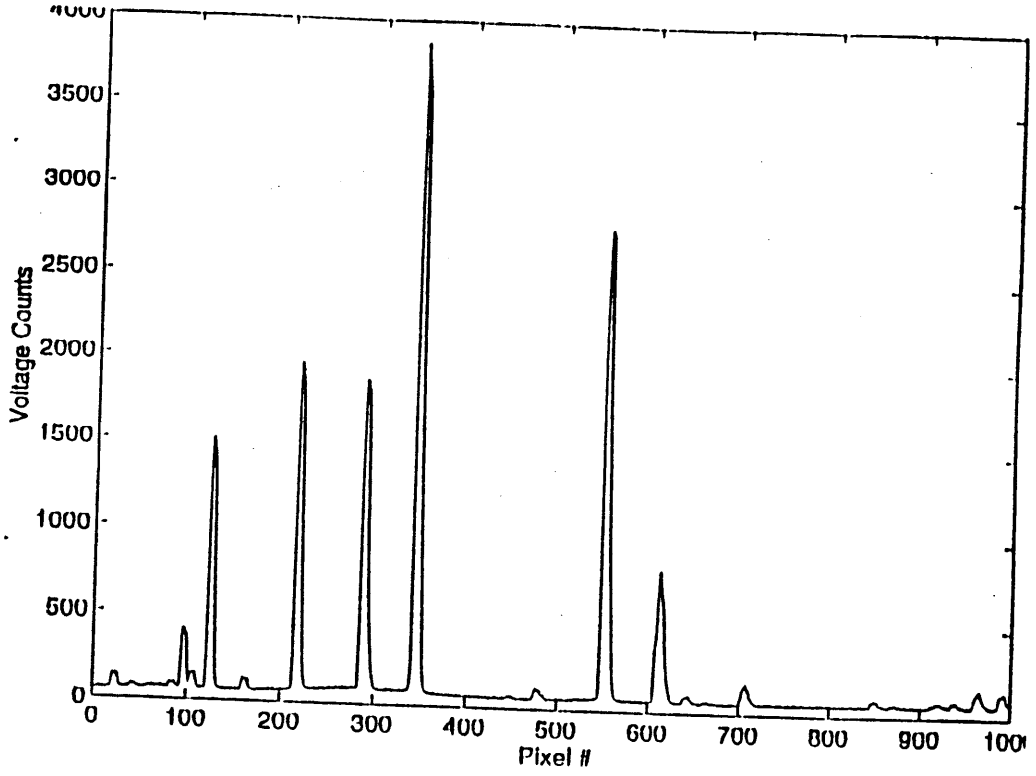

Figure 2-9: Pixels number vs. HgAr emission peaks.

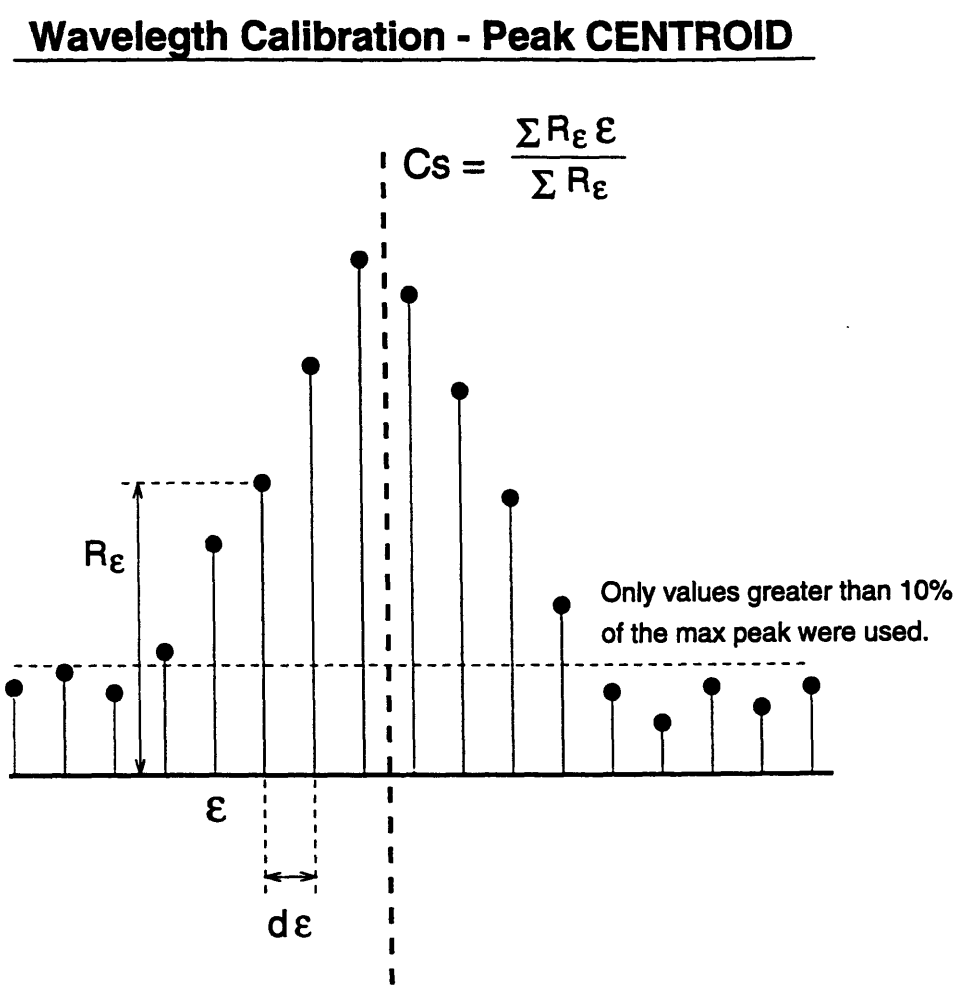

Figure 2-10: Definitions for sub-pixel calculation.

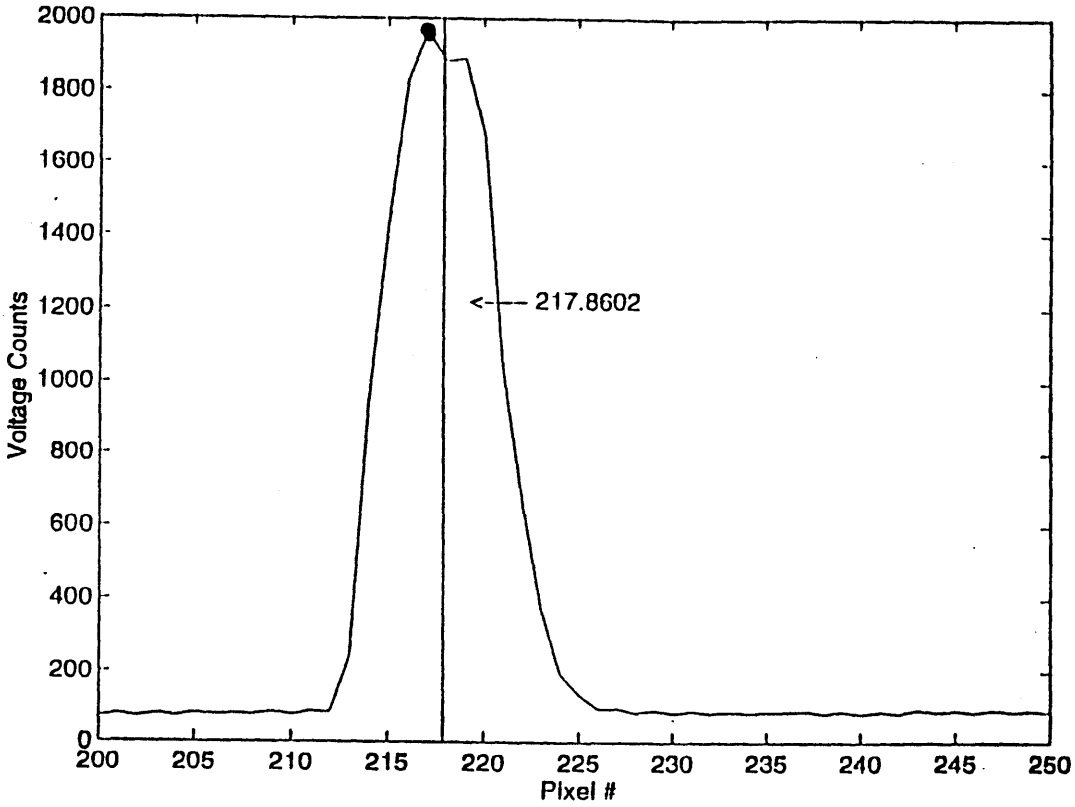

Figure 2-11: Sub-pixel centroid: number 217.8602.

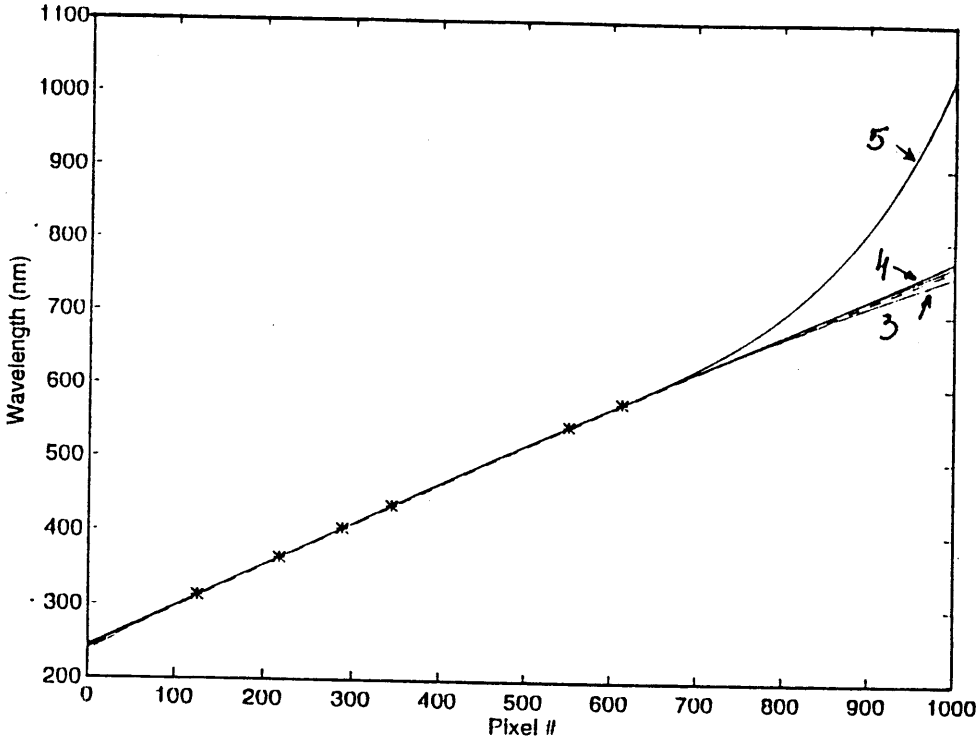

Figure 2-12: 2nd to 5th order polynomials comparison.

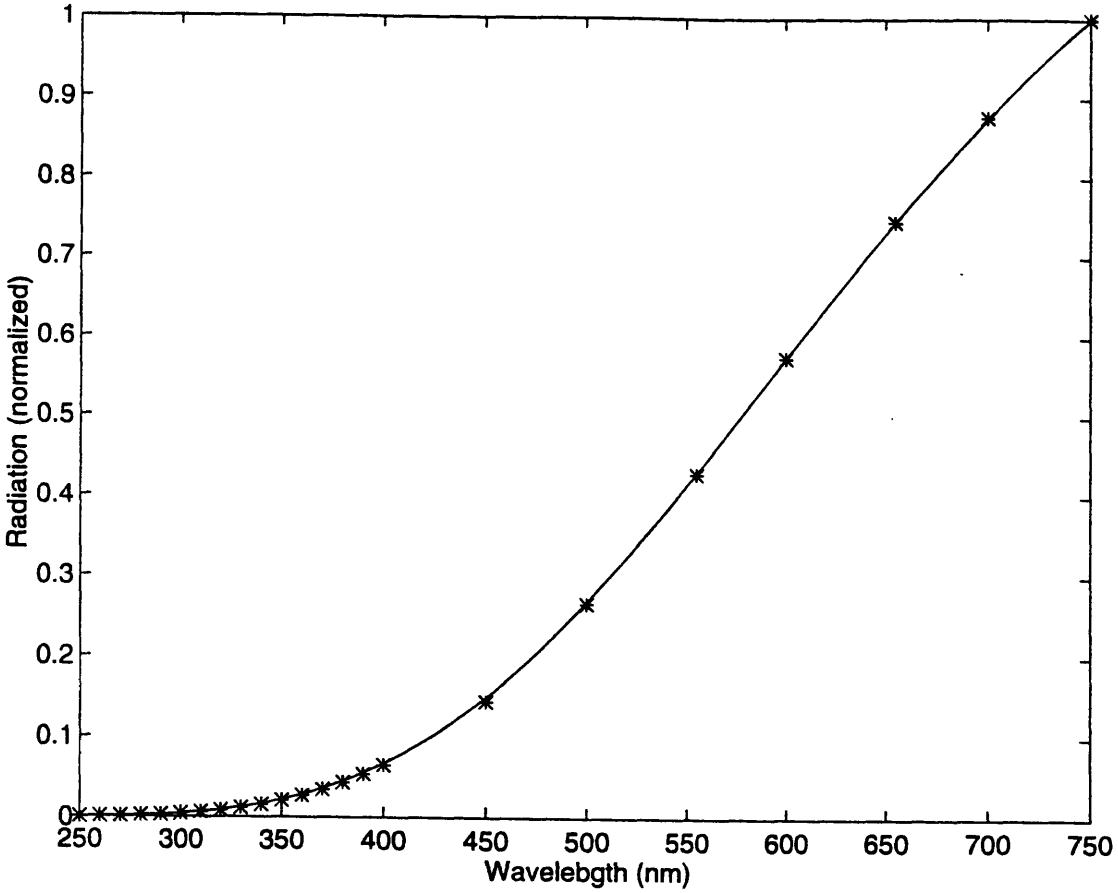

Figure 2-13: Standard calibration lamp data (*) and a $2870^{o}K$ black body radiation curve.

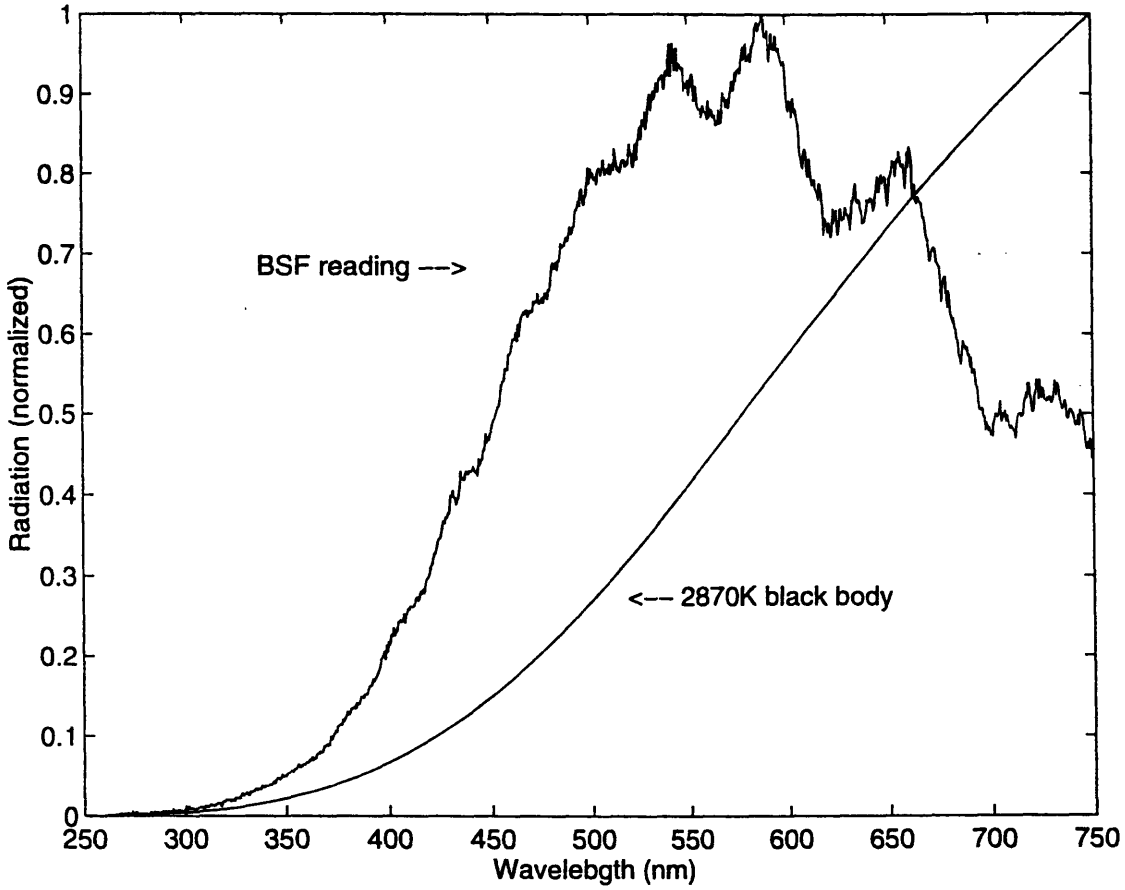

Figure 2-14: Standard calibration lamp reading by the BSF compared with a $2870^{o}K$ black body radiation curve.

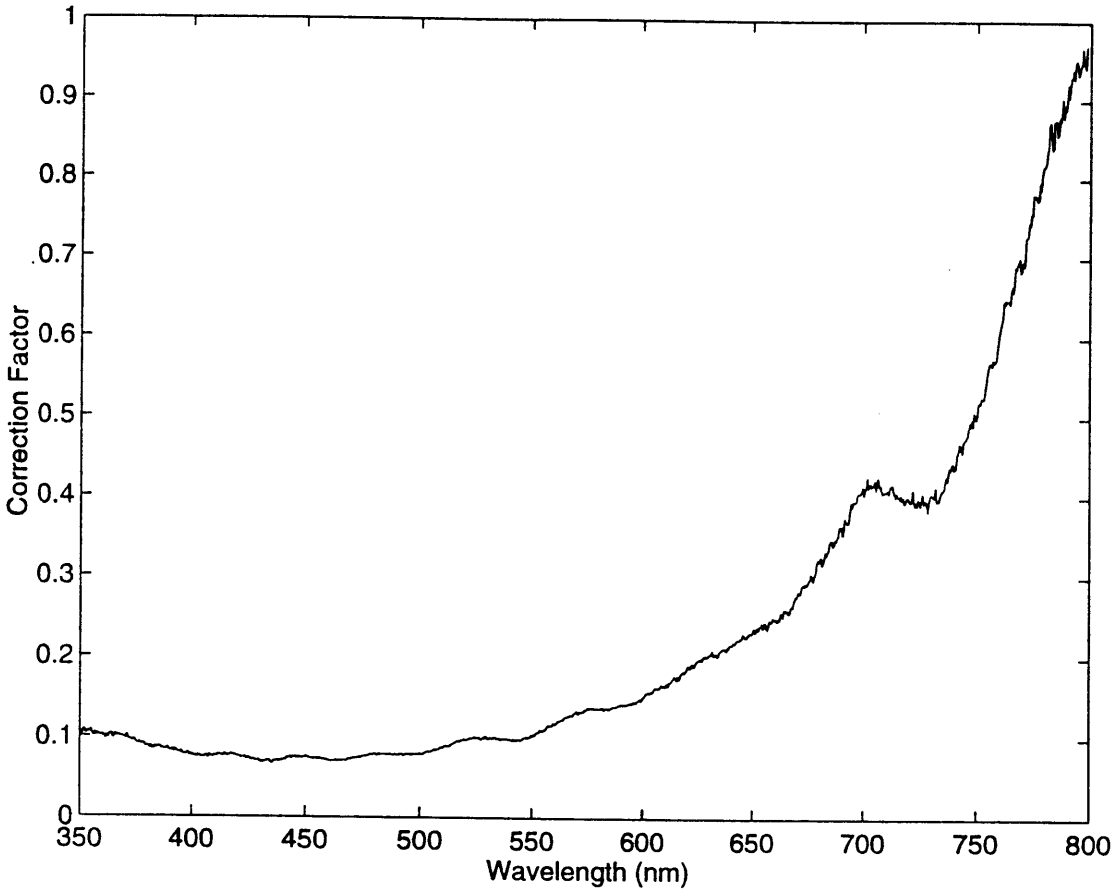

Figure 2-15: The spectral radiation correction curve for the BSF.

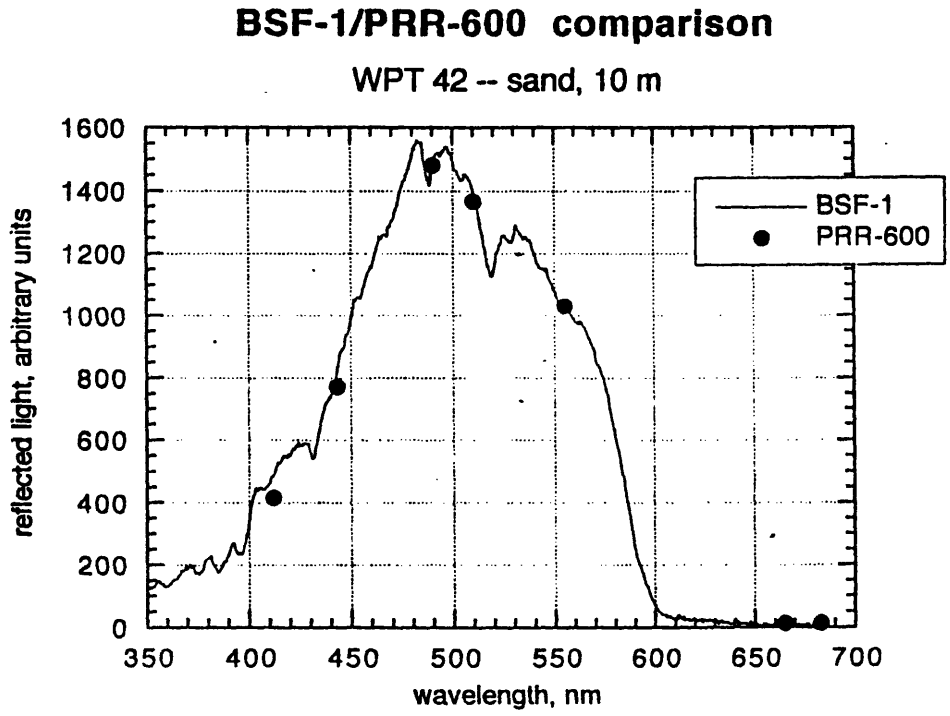

Figure 2-16: Comparing normalized readings of the BSF and PRR600 measuring sand bottom at 10m of sea water.

Chapter 3

True reflectance of fluorescence enhanced colors

3.1 Introduction

The coral fluorescence phenomenon is known for many years now: certain coral species fluoresce when illuminated with UV light (examples: *Ricordea florida, Montastrea annularis*). They also fluoresce while illuminated by white light, but the human eye can not detect this signal, since it is overwhelmed by the reflected light. The meaning of the coral fluorescence is still not completely clear. Can we learn anything about the coral health, age, "mood" by its optical signature? Is the fluorescence mechanism some kind of protection mechanism that evolution had developed in corals to protect them from UV radiation? Or maybe it is just a side-effect that doesn't really have any significant information about the coral biology.

Nevertheless, even without having the answers to the above questions, the fluorescence is there, and thus, when detected, can be used for remote sensing purposes. For example, if one is interested in the coral coverage of a given location, the fluorescence signal can be used to separate corals from sand, rocks or vegetation. The next section is a step towards using the signal coming from corals for remote sensing. An experimental method is presented to separate the reflectance and fluorescence portions of a signal received by an optical detector.

The special characteristics of fluorescent materials do not lend them to simple spectral reflection or transmission measurements primarily because their spectra is directly related to the illumination of the sample. This can be seen in the equation:

$$S(\lambda) = R(\lambda) + F(\lambda)/E(\lambda). \tag{3.1}$$

where

$S(\lambda)$ The measured spectral radiance curve.

$R(\lambda)$ True reflectance curve of the surface.

$F(\lambda)$ The fluorescence signal emerging from the sample.

$E(\lambda)$ The power incident upon the sample.

which says that the spectral radiance factor $S(\lambda)$, is composed of a portion $R(\lambda)$, usually called true reflectance, similar to non-fluorescent colors and another portion which is the fluorescence contribution to the apparent color of the sample. This portion depends on the illumination impinging on the sample, because fluorescence excitation depends on spectral energy distribution of the incoming light.

When trying to analyze a signal that originates in a fluorescing surface (as in the case of remote sensing of coral reefs), it is important to analyze the effect of the different contributors to the signal. Since illumination conditions will vary as a function of time of day, clouds etc. we expect the same coral to produce different signals as a result of the different lighting conditions. While reflectance characteristics are highly dependent on the angle of incident of the incoming light and the angle at which the detector is pointing at the sample, fluorescence is a *Lambertian* (diffused) type of radiation. The above explains the need to separate the signal read from a coral to its true reflectance and fluorescence components. In this section I present an experimental method to determine a true reflectance curve for a fluorescing surface. This method (please refer to ref. [12]) originally was developed for measuring fluorescence dyes in white fabrics, for the textile industry. Later I present a way to improve the method, and apply it to *in situ* field measurements, using the BSF.

3.2 Theory of Method

The method described below enables the true reflectance curve to be determined by calculations. Required data are the spectral radiance curves with two different light sources, and a single wavelength reading taken with a light source, through a fluorescence-killing filter. The two light sources should differ considerably in their ability to induce fluorescence. It is recommended that the first light source would be a white light source (daylight, for example), and the second be the same source through an appropriate fluorescence-weakening filter of known transmission.

In Fig. 3-1 the spectral radiance curve of a fluorescent substance is shown schematically by the solid line ABC, with the emission peak at B. The true reflectance curve is the dashed line ADEC. The reflectance curve of the uncolored substrate is the dot-dash line FGEC. The area ABCEDA is symbolic of fluorescent energy; the area FGEDA of absorbed energy, which is the source of the fluorescence energy. In the wavelength range A to E, simultaneous absorption of exciting energy and emission of fluorescing energy is occurring. This region of the spectrum is called the cross over region.

If a sharp cutoff filter is used, that completely eliminates wavelengths below E, there is no energy reaching the sample that would excite fluorescence, and the true reflectance curve at wavelengths longer than E can be determined. Lets call such a filter a fluorescence-killing filter. On the other hand, the true reflectance curve at wavelengths lower than A can be read directly without a filter, since there is no fluo-

rescence in that region. Accordingly, it is in the crossover region that determination of true reflectance curves is not easy.

The following is the traditional approach as presented in ref. [12]. In the next section I will present a modification for this approach:

For proper use of the method described here, a true reflectance reading at at least one wavelength with the use of fluorescence-killing filter is required. The calculation is made, as will be shown shortly, with the use of the shortest wavelength reflectance reading possible. To be suitable the reading must be made at a wavelength as close as possible to the fluorescence peak. In Fig. 3-1, lines I II III and IV represent schematic transmission curves of sharp cutoff filters. The filters represented by lines I and II do not completely eliminate fluorescence, since the cutoff is occurring to the left of point E and some fluorescence exciting radiant energy is getting through.The filter represented by curve IV does eliminate all fluorescence, but the reading of the lowest wavelength true reflectance value must be taken somewhere between point C and line IV. In this region the fluorescence is not very strong, and the difference between the reading with and without the fluorescence killing filter (somewhere on curves EC and BC, respectively) is not too great, resulting in decreased precision. Also, the cutoff at this high a wavelength limits the region in which direct true reflectance readings may be obtained. Curve III represents the preferred fluorescence killing filter, since the curve is to the right of point E, but far enough to the left to obtain a large difference between the reading with and without fluorescence. In practice, the proper fluorescence-killing filter is determined by trial and error (this one of the main points that I suggest to improve, in the next section).

Next, another reading is needed, using a fluorescence weakening filter. We need to choose the proper fluorescence weakening filter. The filter should eliminate most of the fluorescence, but the cutoff wavelength should still be low enough that the full spectral radiance factor curve in the crossover region should be plottable. In Fig. 3-1, the filter represented by line II would not be suitable as a fluorescence weakening filter, although it eliminates most of the fluorescence, it does not enable plotting of the spectral radiation curve down to point A. The preferred fluorescence-weakening filter is represented by line I; it doesn't eliminate as much of fluorescence as does filter II, but the curve can be plotted down to point A.

The derivation of the formula used for calculating the true reflectance curve in the crossover region from the data obtained as describe above, is as follows:

$E_1(\lambda)$ relative spectral power distribution of light source no. 1.

$E_2(\lambda)$ same for source no. 2.

k_1 constant (independent of wavelength) that converts relative spectral power distribution of light source no. 1 to absolute power values.

k_2 same for source no. 2.

$T(\lambda) = E_1(\lambda)/E_2(\lambda)$.

$F(\lambda)$ fluorescence emission curve of sample irradiated with light source no. 1, absolute power values.

k_f constant (independent of wavelength) that converts the $F(\lambda)$ values to the fluorescence emission curve (absolute) of sample irradiated with light source no. 2.

The same relative curve shape for fluorescence emission, under the two light sources is assumed.

The measured spectral radiance factor for the sample irradiated by light source no. 1, denoted by $S_1(\lambda)$, is given by

$$S_1(\lambda) = R(\lambda) + F(\lambda)/k_1 E_1(\lambda). \tag{3.2}$$

The corresponding quantity for light source no. 2 is

$$S_2(\lambda) = R(\lambda) + k_f F(\lambda)/k_2 E_2(\lambda), \tag{3.3}$$

but since $E_2(\lambda) = T(\lambda)E_1(\lambda)$, we have

$$S_2(\lambda) = R(\lambda) + k_f F(\lambda)/k_2 T(\lambda) E_1(\lambda). \tag{3.4}$$

Lets eliminate $F(\lambda)/E_1(\lambda)$ between eqs. (3.3) and (3.4) to obtain:

$$R(\lambda) = [S_2(\lambda)T(\lambda)k_2 - S_1(\lambda)k_1 k_f]/[k_2 T(\lambda) - k_1 k_f]. \tag{3.5}$$

The constant k_f is directly proportional to k_2 because, for example, doubling the power of light source no. 2 would double both k_2 and k_f. Similarly, k_f is inversely proportional to k_1. Therefore we have $k_f = kk_2/k_1$, where k represents a new units conversion constant. Substituting this expression for k_f into eq. (3.5), we get

$$R(\lambda) = [S_2(\lambda)T(\lambda) - S_1(\lambda)k]/[T(\lambda) - k]. \tag{3.6}$$

The constant k can be evaluated from the lowest wavelength reading obtained with the fluorescence-killing filter. Let w represent this wavelength, and let $R(w)$ represent the true reflectance reading which was obtained. The spectral radiance factor readings obtained at this wavelength in the course of the measurements with light sources no. 1 and 2, are $S_1(w)$ and $S_2(w)$, respectively. The value of T at this wavelength is $T(w)$. If we write eq. (3.6) for this specific wavelength, and solve for k, we obtain:

$$k = T(w)[S_2(w) - R(w)]/[S_1(w) - R(w)]. \tag{3.7}$$

Equations (3.6) and (3.7) are the working equations that are used in this method. Equation (3.7) is first used to calculate k, and then Equation (3.6) is applied at each other wavelength in the crossover region to calculate $R(\lambda)$. If desired, the calculations can be extended to wavelengths above the crossover region also, in which case they

will duplicate the readings taken directly at these wavelengths with the fluorescence-killing filter. Agreement between the calculated and the measured readings at these wavelengths is a good test of the accuracy of the method.

Note that the two relative power distributions $E_1(\lambda)$ and $E_2(\lambda)$ were eliminated from the equations, and we only use their ratio $T(\lambda)$. If the two light sources that we were using were a single source with and without a fluorescence weakening filter, $T(\lambda)$ is simply the transmission curve of this filter, which is relatively easy to obtain.

Please refer to Ref. [12] for results of testing and applying this method to white cotton samples, dyed with several different fluorescence dye substances. This experimental method show good agreement with reality. However there are a few issues that can be improved in the original method. These improvements are presented in the next section.

3.3 The weak aspects of the method

Although the above method works, and show good results, it still has few weak points that can be improved. Furthermore, for our purposes, it is desirable to be able to use this method for *in situ* measurements, using the BSF as the field instrument. Lets examine the weak points of the method:

Gaining more confidence in the constant k

As suggested in Ref. [12], the constant k is determined by considering only one reading, at wavelength w. Generally, it is better to have a result based on an average of several readings, at different wavelengths.

Selecting a filter

According to Ref. [12], the only data that one has, when trying to decide what filters to use as fluorescence-killing or fluorescence-weakening filters, is the total reflectance curve, which is combined both from the true reflectance and the fluorescence enhancement signal. It is unclear where the fluorescence signal is affecting the reading - thus a trial and error approach is suggested, to find the right filters. It would be beneficial if we could find a better way to estimate what cutoff wavelength these filters should have.

The use of cutoff filters assumes a sharp cutoff wavelength. Since filters do not have an absolutely sharp curve (there is always a slope associated with the transition from low transmittance to high transmittance), there is a transition region, in which the filter slope can affect the accuracy of the results. It is preferable not to work in this region, but doing so will limit the range that a filter is covering. It would be nice if our method would not be sensitive to filter selection and characteristics.

Singularity in the crossover region

From examining Eq. (3.6) it is clear that there is a singularity, when the denominator goes to zero. This means that when $T(\lambda) = k$, the method fails. In this case

interpolation technique is used to smooth the curve. It would be nice if we could find a way to calculate the true reflectance curve in all the crossover region, with no singularities.

3.4 Improving the method

In order to overcome few of the above problems, lets consider another piece of available information: the pure fluorescence curve shape of the fluorescing substance in the sample. Say we could measure the signal coming purely from fluorescence. Would it help us in any way?

3.4.1 Determining the constant k

Following the theory presented in the previous section, we notice that the determination of k is recommended at the wavelength w (cutoff of the fluorescence killing filter) to allow best SNR. However, the same constant k should be received if we use a slightly longer wavelength than w in our calculations. Theoretically k should be the same for any $\lambda > w$ that we use. But, the apparent reflectance curve (the curve that we measure from the sample with no filters), and the true reflectance curve (the one that is measured by applying the fluorescence killing filter) are converging together at some $\lambda > w$. Since k is calculated from the difference between these two, its accuracy is affected by the system noise and performance, as the two values are getting closer to one another. This system limitation define a range at which $k$can be calculated. If instead of only looking for k at one wavelength (w) we were to plot k (calculated by Eq. 3.7, but using all the spectrum), we expect a constant value for k from about $\lambda = w$ to a certain wavelength where the sensor noise is taking over, and k has no longer a reliable value. Lets call this noise-limiting wavelength λ_n. If I am right - there should be a range: $w < \lambda < \lambda_n$ where k is constant.

Another important advantage to this method is its non-sensitivity to the killing filter cutoff slope. Relying on w only, requires a sharp cutoff filter. The suggested method is less sensitive to the slope, since we are not looking at a single wavelength.

The above concept was applied to a fluorescent green test surface. In this test the killing fluorescence wavelength cutoff was 530nm (ie $w = 530nm$), and the weakening filter was 475nm. The light source was a tungsten incandescent light bulb. Measurements were taken with an S1000 spectrometer.

As can be seen in Fig. 3-2, there is a region ($530 < \lambda < 560nm$) where the value of k is relatively constant, suggesting that the analysis presented above is accurate, hence increasing the confidence in the calculated value of k.

3.4.2 Choosing filters

Typical fluorescence emission peaks are related to their excitation peaks, as illustrated in Fig. 3-3. The excitation peak is always at a shorter wavelength than the emission

(due to the energy nature of the fluorescence process), and there is an overlapping region where the excitation is decreasing while the emission is rapidly growing. If we had the excitation curve of the fluorescing material which is in the sample, we could choose exactly the desired filters for weakening and killing the fluorescence signal. But, this curve is hard to get, and will require other instruments than the BSF. The use of such instruments, which were not designed for underwater operation, mean that the concept of *in situ* measurements can not be met.

But - the emission curve is relatively easy to get: the signal received from a fluorescing sample when illuminated only by UV light, is combined of two separate peaks: the reflected UV light and the emitted fluorescence. If we block the UV light from getting to the sensor (or simply consider the visible region only, in which case we don't care about the UV signal), we have a curve that was purely generated by fluorescence. This curve and the typical relative position of the excitation curve (Fig. 3-3), give us a hint of what the weakening and killing filters cutoff should be. For the weakening filter we can choose a wavelength in the region where the fluorescence signal is starting to build up, while for the killing filter, we should choose a wavelength longer than the fluorescence emission peak. These two choices give us a starting point to test if our filter selection is appropriate. Although this method is not full proved, it is better than the trial and error method that Ref. [12] suggests.

3.4.3 Calculating true reflectance

Assuming that we have measured $F(\lambda)$, lets examine what can we get from this information.

Define:

$F(\lambda)$ Radiation distribution due to fluorescence. Assume that the shape of this spectrum is independent of excitation wavelength (common assumption for first order approximation).

γ Factor that converts $F(\lambda)$ from relative units to the sample measurement units.

$E_0(\lambda)$ Irradiance hitting the sample.

$E_A(\lambda)$ Irradiance leaving the sample surface.

$R_T(\lambda)$ True reflectance.

$R_A(\lambda)$ Apparent (fluorescence enhanced) reflectance.

Another way of writing Eq. 3.1 is:

$$E_A(\lambda) = E_0(\lambda)R_T(\lambda) + \gamma F(\lambda), \tag{3.8}$$

or:

$$R_A(\lambda) = R_T(\lambda) + \gamma \frac{F(\lambda)}{E_0(\lambda)}. \tag{3.9}$$

We can define the last term as the fluorescence enhancement,

$$R_F(\lambda) = \gamma \frac{F(\lambda)}{E_0(\lambda)}. \tag{3.10}$$

To find γ we can use the measured information from the sample:

$$\gamma = \frac{(R_A - R_T)E_0}{F}. \tag{3.11}$$

Theoretically, we need only one data point (wavelength) to determine γ ($\lambda = w$ is a reasonable choice), but following the same consideration as in the case of k, we would prefer to have a region of wavelengths to calculate γ. We get this region by using Eq. 3.11, not at a single wavelength, but for all λ in the crossover region, where we expect to find a relatively constant value for γ in some region before w (as can be seen in Fig. 3-4).

The factor γ is a constant that applies to all wavelengths. Once we know it we can calculate:

$$R_T(\lambda) = R_A(\lambda) - \gamma \frac{F(\lambda)}{E_0(\lambda)}. \tag{3.12}$$

where R_A, F, E_0 were measured, and γ calculated. This gives us the true reflectance curve that we were looking for, without the singularity that we had in the traditional method. Thus we can get the full crossover region covered.

The quality of the results highly depends on the fluorescence signal. In order to cover the crossover region, we must separate completely between the UV light that we used for exciting the fluorescence and the fluorescence signal itself. We also need a strong and clean fluorescence signal. Since we did not have a complete separation when the test were made in the lab, there is a small region where results are not perfect. Performances of the optical unit resulted in a very weak fluorescence signal, that caused a noisy signal. Since the measured signal (F) is scaled to convert to the same units as the sample measurements (γ), the noise is scaled too, and we ended having a relatively noisy signal.

As mentioned in the previous section, the optical system is undergoing major improvements, that are believed to enable getting a better and cleaner fluorescence signal. New UV blocking filter was found, and will contribute to a better separation from the UV signal. Final testing and proving of the improved method will take place after incorporating all the improvements in the BSF, and applied to collected data during the next field trips. This work will be continued into a wider research, and will be completed as a part of my PhD thesis in the future.

3.5 Figures - chapter 3

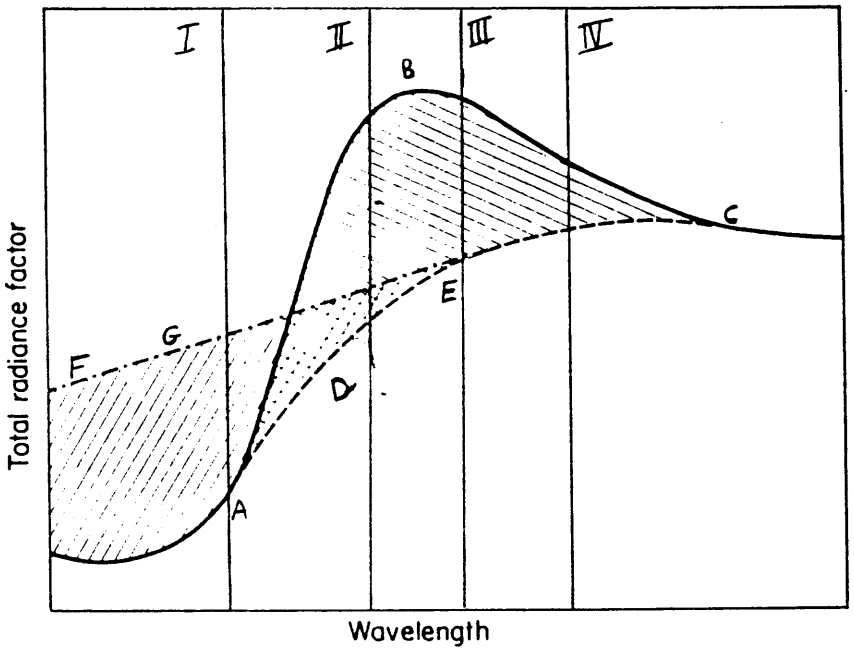

Figure 3-1: Schematic representation of spectral radiance of a fluorescence substance.

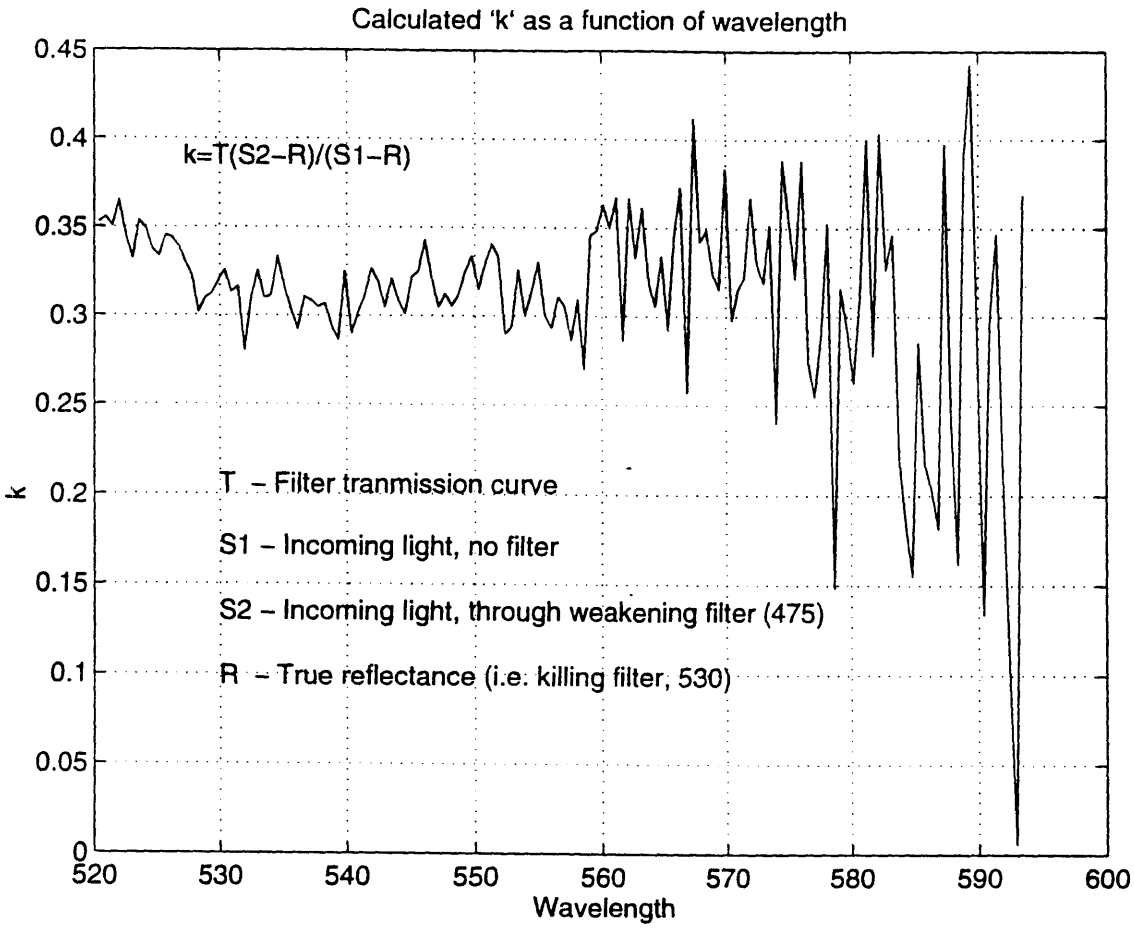

Figure 3-2: Wavelength range to determine the constant k.

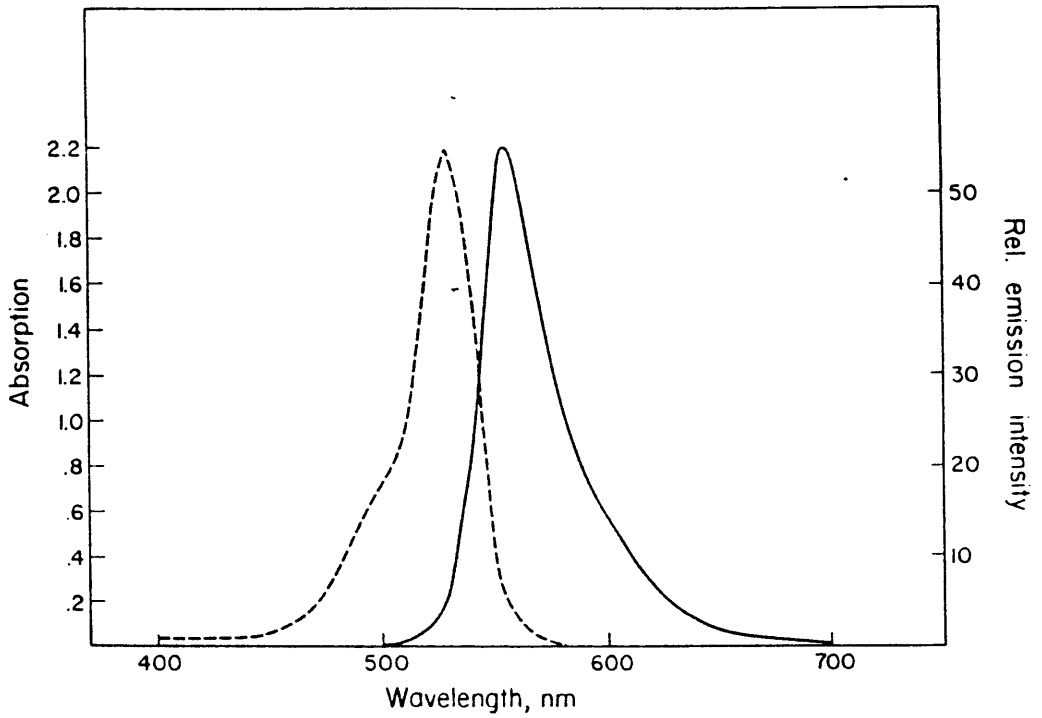

Absorption and emission spectra of a rhodamine solution (10^{-4} M in H_2O).

Figure 3-3: Typical excitation (dashed) and emission (solid) curves for fluorescing materials.

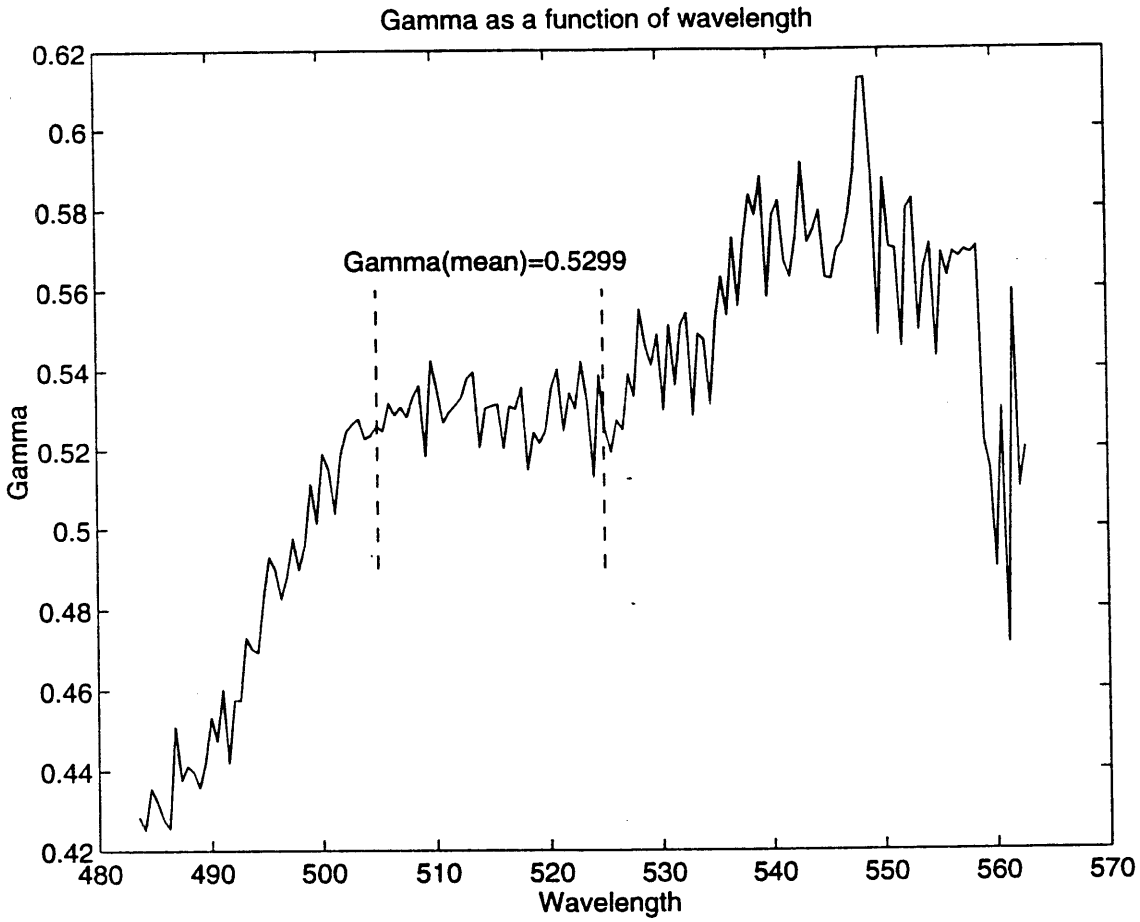

Figure 3-4: γ - fluorescence conversion factor.

Chapter 4

Summary

Remote sensing of the aquatic medium is a challenging problem that involves understanding both the technical issues that an optical sensor designer faces, and the specific problems that are related to the aquatic environment.

After presenting the available, state-of-the-art technology for hyperspectral remote sensors, we could identify that the sensor technology is advanced compared with our capability to interpret and analyze the data received from such a system. Theoretical and analytical background is needed to help scientists to make good use of the collected data. A wide and detailed library of optical signatures of bottom entities is needed for productive classification of bottom entities.

A background study of the unique optical properties of the aquatic environment was presented. This study not only showed the complexity of the issue, but also reveled its empirical nature, suggesting that more research efforts will be made in the general field of ocean optics, before a pure remote sensing models could be applied. Such efforts are being done in many research centers (for example - in the University of South Florida), which hopefully will contribute to the ability to model and analyze the signal recorded by a remote sensing system.

An underwater spectrometer (the Benthic SpectroFluorometer) was presented in the second part of this work. The BSF calibration process for wavelength, dark current correction and radiometric measurements was explained in details. The BSF was tested and compared to a commercial spectrometer (PRR-600), and was found to perform accurately. Although the BSF is still undergoing development and improvements, we consider it as a working instrument, that can be used to collect *in situ* reflectance and fluorescence measurements from objects of interest. Future improvements for the instrument are mainly meant to improve maintenance and human interface. The main use of the BSF at the moment is investigating optical properties of the coral reef.

As a first step to analyze the signal received from coral tissues, an experimental method to calculate true reflectance curves was presented. The method (originally introduced in the 1970's), is a proved and working one, but it has few weak elements:

- The confidence in the calculated constant k.
- The difficulties in choosing the appropriate filters.
- The sensitivity of the results to the cutoff slopes of the filters.
- The singularity that prevents from covering all of the cross-over region.

A simple data manipulation process is suggested to increase confidence in the calculated constant k. A new idea was introduced: to use a pure fluorescence signal as a means to overcome few of the above weaknesses. It can help choosing the right filters, reduce sensitivity to the filter slopes and overcome the inherent singularity in the original method. The new technique can not harm the results compared with the old method, it can only be as good - or better, since the same data needs to be collected in both methods, and thus both methods can be applied.

The BSF will be used to collect optical data this summer in few field trips. Some of the data will be used to calculate true reflectance curves of coral species of interest. Other data will be used to investigate the knowledge that can be gain from optical measurements of coral tissues. The results of this work will be the base to a continuing effort to analyze the aquatic environment, and build an analytical model for remote sensing of the aquatic medium in general, and the coral reef specifically. Hopefully this research effort will lead to my PhD thesis.

The End

Bibliography

[1] John T. O. Kirk Light and photosynthesis in aquatic ecosystems University Press, Cambridge 1986.

[2] Smith, R. C., and K. S. Baker. *Optical properties of the clearest natural waters.* Appl. Op. (20), 1981.

[3] Thomas McCord, Gregory Mooradian ,Jessica Sunshine and more Hyperspectral Remote Sensing for Maritime Applications: Phase I. *SETS Technology, Inc.*, 1994.

[4] Sarah A. Green, Neil V. Blough and Anthony Vodacek An experimental model of the solar stimulated flourescence of chromophoric dissolved organic matter. *Limnology and Oceanography*, 39(1), 1994.

[5] Peacock, Carder, Davis and Steward Effects of fluorescence and water Raman scattering on models of remote sensing reflectance. In *Ocean Optics (10)*, pages 303–319. 1990.

[6] Thomas M. Lillesand and Ralph W. Kiefer Remote Sensing and Image Interpretation. *John Wiely and Sons, Inc. 1987*

[7] Morel, A. and Raymond C. S. Terminology and units in Optical Oceanography *Marine Geodesy, vol. 5, no. 4, 1982*

[8] Scopatz, S., Neel G., Romesburg E. and Zivitz M. Calibrating a detector array based spectroradiometer with sub-pixel precision. *SPIE vol. 1055, 1989*

[9] Smith, W. M. and Biggar, F. S. Calibration and performance evaluation of a portable shortwave infrared spectrometer. *Optical Engineering, vol. 33 no. 11, Nov. 1994*

[10] Giles, W. J. and Voss, J. K. Submerged reflectance measurements as a function of visible wavelength. *SPIE vol. 1537, 1991*

[11] OPTRONIC laboratories, Inc. Report of calibration, Project No. 903-395, June 5, 1995.

[12] Allen E. *Separation of the Spectral Radiance Factor Curve of Fluorescent Substances into Rflected and Fluoresced Components.* Appl. Op. (Vol. 12, No. 2), Feb. 1973.

[13] Simon T. Frederick *Serial filter analysis of fluorescent materials.*

[14] Mobley, D. C. Light and Water *Academic Press, 1994*

[15] Frankel, E. Ocean Environmental Managment *Prentice-Hall, Inc. 1995*

[16] Boas, L. M. Mathematical Methods in the Physical Sciences *John Wiley and Sons, Inc. 1966*

[17] Sefton, N. and Webster, K. S. Caribbean Reef Invertebrates *Dai Nippon Printing Co., Ltd., Japan 1986*